LIMNOLOGY
and
OCEANOGRAPHY

ASLO

Limnol. Oceanogr. 64, 2019, 2059–2080
© 2019 The Authors. *Limnology and Oceanography* published by Wiley Periodicals, Inc. on behalf of Association for the Sciences of Limnology and Oceanography.
doi: 10.1002/lno.11169

Temporal variability of lagoon–sea water exchange and seawater circulation through a Mediterranean barrier beach

Joseph Tamborski,[1]* **Pieter van Beek**,[1] **Valentí Rodellas**,[2] **Christophe Monnin**,[3] **Erwin Bergsma**,[1] **Thomas Stieglitz**,[2,4] **Christina Heilbrun**,[5] **J. Kirk Cochran**,[5] **Céline Charbonnier**,[6] **Pierre Anschutz**,[6] **Simon Bejannin**,[1] **Aaron Beck**[7]

[1]Laboratoire d'Etudes en Géophysique et Océanographie Spatiales (Université de Toulouse, CNES, CNRS, IRD, UPS), Observatoire Midi Pyrénées, Toulouse, France
[2]Aix-Marseille Université, CNRS, IRD, INRA, Coll France, CEREGE, Aix-en-Provence, France
[3]Géosciences Environnement Toulouse (Université de Toulouse, CNRS, IRD, UPS), Observatoire Midi Pyrénées, Toulouse, France
[4]Centre for Tropical Water & Aquatic Ecosystem Research, James Cook University, Townsville, Queensland, Australia
[5]School of Marine & Atmospheric Sciences, Stony Brook University, Stony Brook, New York
[6]Environnements et Paléoenvironnements Océaniques et Continentaux, Université de Bordeaux, CNRS, Talence, France
[7]GEOMAR Helmholtz Centre for Ocean Research Kiel, Kiel, Germany

Abstract

The subterranean flow of water through sand barriers between coastal lagoons and the sea, driven by a positive hydraulic gradient, is a net new pathway for solute transfer to the sea. On the sea side of sand barriers, seawater circulation in the swash-zone generates a flux of recycled and new solutes. The significance and temporal variability of these vectors to the French Mediterranean Sea is unknown, despite lagoons constituting ~ 50% of the coastline. A one-dimensional $^{224}Ra_{ex}/^{223}Ra$ reactive-transport model was used to quantify water flow between a coastal lagoon (La Palme) and the sea over a 6-month period. Horizontal flow between the lagoon and sea decreased from ~ 85 cm d^{-1} during May 2017 (0.3 m^3 d^{-1} m^{-1} of shoreline) to ~ 20 cm d^{-1} in July and was negligible in the summer months thereafter due to a decreasing hydraulic gradient. Seawater circulation in the swash-zone varied from 10 to 52 cm d^{-1} (0.4–2.1 m^3 d^{-1} m^{-1}), driven by short-term changes in the prevailing wind and wave regimes. Both flow paths supply minor dissolved silica fluxes on the order of ~ 3–10 mmol Si d^{-1} m^{-1}. Lagoon–sea water exchange supplies a net dissolved inorganic carbon (DIC) flux (320–1100 mmol C d^{-1} m^{-1}) two orders of magnitude greater than seawater circulation and may impact coastal ocean acidification. The subterranean flow of water through sand barriers represents a significant source of new DIC, and potentially other solutes, to the Mediterranean Sea during high lagoon water-level periods and should be considered in seasonal element budgets.

Subterranean water exchange between coastal lagoons and the coastal ocean remains severely understudied, despite coastal lagoons representing ~ 13% of the global coastline (Barnes 1980; Santos et al. 2012). This underground lagoon–sea water exchange depends on the hydraulic gradient between the two water bodies (pressure) and the properties of the barrier which separates them, including sediment porosity and permeability. Separately, tides and waves can drive large volumes of seawater into permeable beaches, resulting in a seawater circulation cell (Li et al. 1999; Robinson et al. 2007; Xin et al. 2010). Pore waters from either flow path can obtain a unique geochemical signature from early diagenetic nutrient mineralization (Anschutz et al. 2009; Santos et al. 2009; Charbonnier et al. 2013; Goodridge and Melack 2014) and/or sediment weathering (Schopka and Derry 2012; Ehlert et al. 2016). Lagoon–sea water exchange and seawater circulation flow paths are therefore a potential source of both recycled and new chemical elements to the coastal ocean; thus, it is necessary to understand the time-scale of each flow path to properly evaluate chemical fluxes (Tamborski et al. 2017). Each of these flow paths may be characterized as a type of submarine groundwater discharge (SGD), broadly defined as "any

*Correspondence: jtamborski@whoi.edu

This is an open access article under the terms of the Creative Commons Attribution License, which permits use, distribution and reproduction in any medium, provided the original work is properly cited.

Additional Supporting Information may be found in the online version of this article.

[a]Present address: Department of Marine Chemistry and Geochemistry, Woods Hole Oceanographic Institution, Woods Hole, Massachusetts

and all flow of water on continental margins from the seabed to the coastal ocean, regardless of fluid composition or driving force" (Burnett et al. 2003).

Lagoon–sea water exchange has been documented along sandy barrier beaches in Fire Island, New York (Bokuniewicz and Pavlik 1990), Florida Bay (Corbett et al. 2000; Chanton et al. 2003), Sapelo Island, Georgia (Evans and Wilson 2017), Malibu Bay, California (Dimova et al. 2017), Venice Lagoon (Italy) (Rapaglia et al. 2010), Patos-Mirim Lagoon (Brazil) (Windom et al. 2006; Niencheski et al. 2007), and the Great Barrier Reef (Australia) (Santos et al. 2010). Chemical fluxes associated with this SGD have only been reported for Malibu Bay, Venice Lagoon, Patos-Mirim Lagoon, and the Great Barrier Reef (Windom et al. 2006; Niencheski et al. 2007; Rapaglia et al. 2010; Santos et al. 2010; Dimova et al. 2017). All of these study sites are situated along areas with significant tidal ranges to produce water level, and therefore pressure, variations. For example, the tidal range of Venice Lagoon (neap = 0.3, spring = 1.2 m), situated along the northern Adriatic Sea, was found to drive SGD flow rates up to 140 cm d^{-1} through highly permeable paleochannels (Rapaglia et al. 2010). However, little to no information exists on the magnitude and temporal variability of this lagoon–sea water exchange flow path to microtidal coastal environments. This is the case of the French Mediterranean coastline, where tides are insignificant (~ 20–30 cm), and there is a striking succession of coastal lagoons of various sizes that are separated from the sea by only narrow sand barriers, constituting ~ 50% of the coastline (Stieglitz et al. 2013).

Seawater circulation through permeable sandy beaches is primarily driven by tides and waves (Li et al. 1999; Santos et al. 2012) and may be regarded as a net zero water flux. Such a process can induce large volumetric fluxes of circulated seawater in high-energy environments, as observed, for example, in Long Island Sound, New York (Tamborski et al. 2017) and the French Aquitanian Coast (Charbonnier et al. 2013). Tides are minor along the French Mediterranean Sea, such that wave setup and water level fluctuations are hypothesized to drive a net seaward flowing circulation cell beneath the swash-zone (Sous et al. 2016). The temporal variability of seawater circulation as a vector for solute transport to the French Mediterranean Sea is largely unknown (Tamborski et al. 2018).

The suite of naturally occurring Ra isotopes (^{223}Ra = 11.4 d, ^{224}Ra = 3.66 d, ^{226}Ra = 1600 yr, ^{228}Ra = 5.75 yr) and ^{222}Rn (3.83 d) have unique half-lives, which enable tracing porewater flow paths of varying time-scales (Rodellas et al. 2017). These radionuclides are supplied to pore fluids by the decay of their surface-bound parent isotope through alpha recoil and are thus dependent upon sediment grain-size, U/Th content (Porcelli and Swarzenski 2003; Porcelli 2008), and Fe/Mn-oxide surface coatings (Dulaiova et al. 2008; Beck and Cochran 2013). Ra isotopes are primarily adsorbed onto sediment surfaces at low ionic strengths and are partially released into solution at higher ionic strengths due to surface-competition displacement from cations (Webster et al. 1995; Gonneea et al. 2013). Radionuclides can be used in simplified systems to estimate one-dimensional (1-D) advection or diffusion (horizontal or vertical), when the above-mentioned variables are well-constrained (Krest and Harvey 2003; Smith et al. 2008; Michael et al. 2011).

In this study, we use the term "lagoon–sea water exchange" to refer to the lateral transport of pore waters through a permeable barrier beach, mainly driven by water level differences across the barrier. Separately, we use the term "seawater circulation" to refer to coastal Mediterranean seawater that has been driven into permeable sediments by physical forcing mechanisms, including waves. Using radionuclide tracers and physical observations, we assess the relative magnitude and monthly temporal variability of (1) lagoon–sea water exchange through the barrier beach and (2) seawater circulation through the swash-zone. In addition, we provide a first-order approximation of solute fluxes (dissolved inorganic carbon [DIC], dissolved silica [DSi], and Ba) driven by these two separate processes.

Study site

La Palme lagoon is a small coastal lagoon (~ 5 km) situated along the French Mediterranean coastline, adjacent to the barrier beach La Franqui (Fig. 1). The southern basin of La Palme lagoon is a shallow sandy basin (20–50 cm water depth) that has limited surface water exchange with the northern basin of the lagoon through a constructed railway dike and bridge and is often partially dry during the summertime. The lagoon may exchange with the Mediterranean Sea via a small inlet which is naturally opened from high-energy storm-events. Tides in this region are minor (~ 20 cm), such that when the inlet is closed, water level differences between the southern basin of La Palme lagoon and the Mediterranean Sea are mainly driven by changes in precipitation and evaporation. Precipitation is highest during the fall and spring (440 mm total in 2017); evaporation rates typically exceed precipitation rates during the summer (Stieglitz et al. 2013). The beach sediment of La Franqui is a well-sorted medium sand, with a mean grain-size between 200 and 500 μm.

Methods

Field methods

The inlet to the Mediterranean Sea was closed months prior to the start of sampling. A shore-perpendicular transect (T1) was sampled monthly between the southern basin of La Palme lagoon and the Mediterranean Sea during May–September 2017 (Fig. 1). Transect T1 was additionally sampled in November 2017, 4 d after the beach was breached by a storm event, which resumed surficial exchange between the lagoon and the sea. A second transect (T2) was sampled during May 2017 only. Samples along the first transect were evenly spaced 10 m apart; samples from the second transect (~ 250 m north)

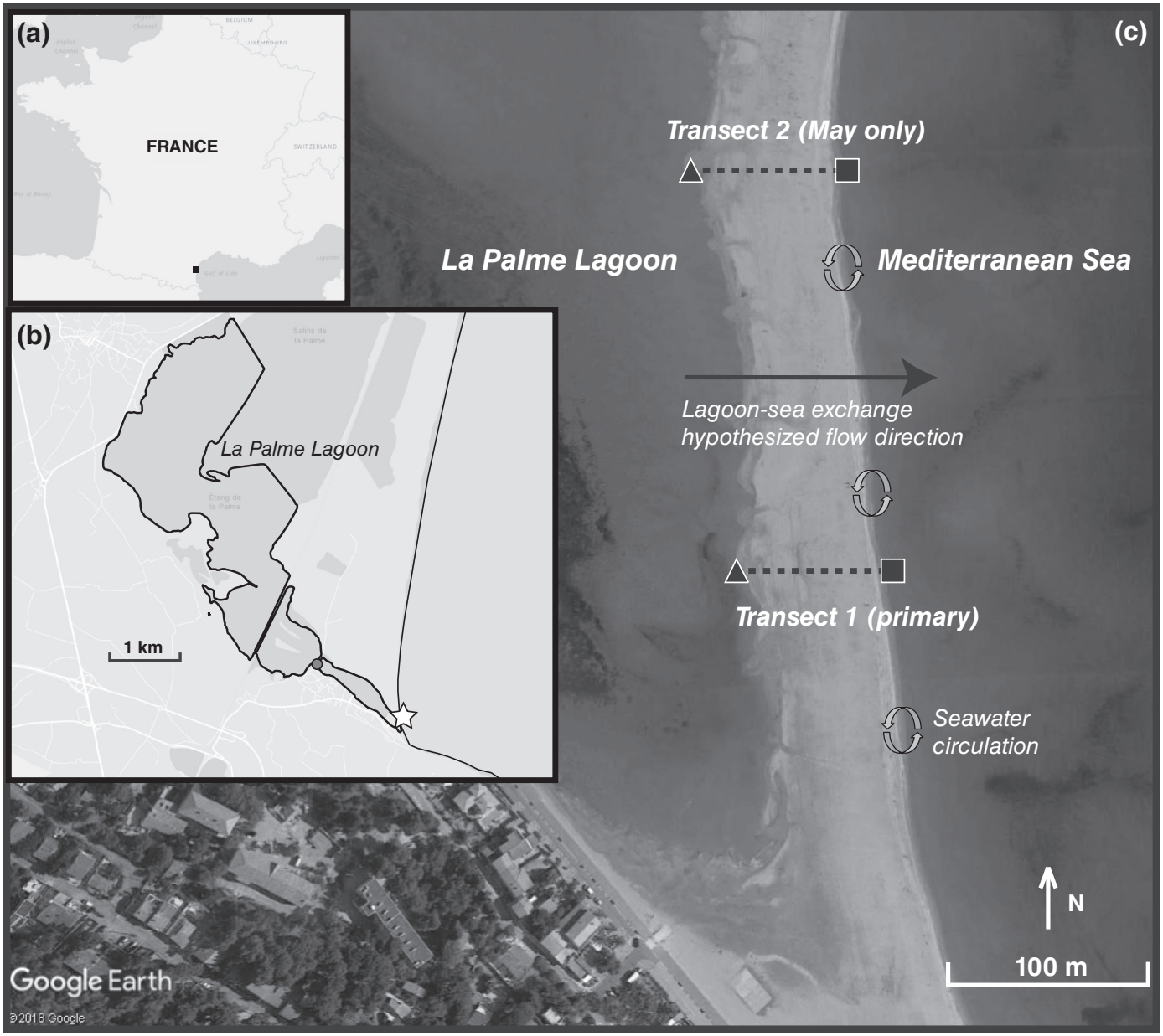

Fig. 1. The study site of La Franqui, located between La Palme lagoon and the Mediterranean Sea (Southern France, inset **a**; black square). The shore-perpendicular transect (Transect 1) was sampled monthly from May to September 2017 and again in November 2017. Transect 2 was sampled during May 2017 only. Google Earth imagery from 14 May 2017 is located approximately at the position of the white star (inset **b**). Lagoon surface-water elevation measurement location is depicted by a circle (inset **b**; data from Parc Naturel Régional de la Narbonnaise en Méditerranée).

were evenly spaced 20 m apart to assess long-shore spatial variability (Fig. 1).

During May, transects were sampled from boreholes that intersected the saturated zone of the beach; the interstitial water that filled the borehole was immediately sampled. For the remaining sampling campaigns (June–November), pore waters were collected using a shielded-screen (Mesh #50 = 297 μm) drive-point piezometer (Charette and Allen 2006) attached to a vacuum hand pump. Samples were acquired at depth intervals of ~ 50, 100, and 150 cm below grade (150 cm for select stations only). Boreholes were dug adjacent to each piezometer sampling location to measure the depth to the water table for all sampling events. During each campaign, lagoon water and Mediterranean Sea surface water endmembers were sampled directly using a hand pump. Salinity, temperature, pH, and dissolved oxygen (DO) were immediately measured for all samples in the field using a calibrated WTW hand-probe (Multi 3430). Bulk sediment samples were collected from several boreholes during May 2017 (~ 50 cm depth). Shore-perpendicular beach topography was surveyed in June

2017 using a real-time kinematic GPS (Trimble). We assume that the June 2017 surveyed topography is representative of May, July, August, and September, a period in which storms (and thus beach erosion and accretion) were minimal. Beach topography was not surveyed in November 2017.

Analytical methods

Sediment

Sediment samples were dried at 80°C for 48 h, and water content loss was measured (triplicate measurements) to calculate sediment porosity, assuming a mineral grain density of 2.65 g cm^{-3} and corrected for sea salt. Bulk sediment samples were sealed for > 3 weeks and counted on a semiplanar Canberra Ge detector at 352 keV (^{214}Pb), 583 keV (^{208}Tl), and 911 keV (^{228}Ac) to determine the total (surficial + lattice-bound) activity of solid-phase ^{226}Ra, ^{228}Th, and ^{228}Ra, respectively. IAEA 300 and NIST Material 4350B sediment were used to determine the semiplanar detector counting efficiencies.

Sediment samples were additionally measured in a radium delayed coincidence counter (RaDeCC) system (Moore and Arnold 1996), to determine the amount of surface-exchangeable ^{223}Ra and ^{224}Ra produced by ^{227}Th and ^{228}Th present on sediment surfaces (Sun and Torgersen 1998*b*). The number of alpha decays to produce Ra and Rn isotopes is different; this can result in a slightly different rate of recoil supply of Ra (ϵ) to that of Rn. In the ensuing analyses, we assume $\epsilon = 1.0$ (Krishnaswami et al. 1982, 1991). Therefore, we assume that all ^{219}Rn and ^{220}Rn diffused into the circulating He gas loop of the RaDeCC system are produced by ^{223}Ra and ^{224}Ra decay on sediment surface-exchangeable sites. Radon emanation was measured on the sediment using the column cartridges traditionally used for Mn-fiber measurements. Using the traditional column cartridge, we are able to measure a larger volume of sediment (> 150 g) in comparison to the chamber developed by Cai et al. (2012). The disadvantage of the traditional cartridge is that its cylindrical geometry is only suitable for sandy sediment, so that the circulating He gas flow is unobstructed. Fine-grained sediment (silts and clays) could impede the He flow, making this method unusable. Bulk sediment samples were partially dried in an oven until a water : sediment ratio of approximately 0.1 was reached, a ratio previously determined to be sufficient for counting sediment samples on the RaDeCC (Sun and Torgersen 1998*a*; Cai et al. 2012). Cartridges were plugged on each end with raw acrylic fiber to prevent any sediment from entering the system. The He flow rate was continuously monitored throughout the measurement period and matched that of typical Mn-fiber measurements (~ 6 L min^{-1}). A replicate set of homogenized sediment ($n = 8$) was spiked with 3.8–57 dpm ^{224}Ra in equilibrium with ^{228}Th (standard addition; triplicate measurements) to determine the detector counting efficiency (Cai et al. 2012; Fig. 2). Sediment column ^{224}Ra counting efficiency was equivalent to that of Mn-fiber measurements (Sun and Torgersen 1998*b*), and therefore, we assume the same detector efficiency as Mn-fiber measurements for both ^{224}Ra and ^{223}Ra. The importance of sample load was tested to determine the effect of helium "channeling" (Cai et al. 2012), with varying sediment loads of 29–167 g ($n = 7$; triplicate measurements).

Ra distribution coefficient (K_D) experiments were run on sediment samples from two locations (5-PW5-A and 5-2-PW3-A) to determine the Ra partition coefficient (K) for water salinities of 27 and 38 (representative of salinities measured in beach pore waters), following established protocols for such measurements (e.g., Fisher et al. 1983; Roberts et al. 2009). Briefly, these involve suspending the material of interest (in this case, beach sand) in a solution containing the element for which the distribution coefficient is to be determined, under conditions of in situ pH and salinity. After equilibration, generally within ~ 48 h, the fractions of tracer on the sediments and in solution are measured. Sediments were first gamma counted (as noted above) to determine the initial activity of ^{226}Ra from the 352 keV ^{214}Pb photopeak. For each sediment sample, a ^{226}Ra tracer (~ 20 dpm) was added to 100 mL of Ra-free water containing ~ 11 g (salinity of 27) or ~ 20 g of sediment (salinity of 38). The pH of each solution was ~ 7.5 after addition of the ^{226}Ra tracer, and no adjustment was made to alter pH for the experiments. Samples were allowed to equilibrate for ~ 5 d with frequent stirring. At the end of the experiment, the water was decanted off and the sediment was rinsed with small portions of distilled water to remove any residual tracer solution. The sediment was dried and recounted to determine the new ^{226}Ra activity. The activity of ^{226}Ra adsorbed onto the sediment was calculated as the excess ^{226}Ra (above the intrinsic ^{226}Ra activity in the sample) multiplied by the mass of sediment used in the experiment (Eq. 1). K_D was calculated as:

$$K_D = \left[\frac{\text{dpm } ^{226}\text{Ra adsorbed}}{\text{dpm } ^{226}\text{Ra in solution}}\right] \Big/ C_p \quad (1)$$

where C_p = g sediment per mL of solution. ^{226}Ra was used for these experiments, and because the sediments contained natural ^{226}Ra, this fraction was subtracted to determine the partitioning of Ra between solution and solid at the end of the experiment. The solid phase at the start of the experiment comprised several fractions of "natural" ^{226}Ra: (1) in the mineral structure, (2) originally adsorbed onto the sediments, and (3) originally dissolved in wet sediment pore water (and subsequently adsorbed onto the sediments after drying). All three fractions were effectively measured via the gamma spectrometric measurements of ^{226}Ra before the start of the sorption experiments.

Radium and radon equilibration experiments were also conducted to estimate the production and partitioning of ^{223}Ra, ^{224}Ra, and ^{222}Rn from sediments. For ^{223}Ra and ^{224}Ra, ca. 1000 g of sediment was added into a 6-liter plastic container, to which ca. 400 mL of water was added, for a water

salinity of 27 and 38 (representative of salinities measured in beach pore waters). The containers were sealed, and after > 7 weeks, the wet sediment was vacuum filtrated to isolate the pore water from the sediment. MnO_2-coated acrylic fibers were subsequently introduced to the extracted solution, partially rinsed, and analyzed on a RaDeCC system. For ^{222}Rn, ca. 200 g of dry sediment was added into a 500-mL gas-tight bottle, which was then completely filled with Ra-free lagoon water (salinity of 38; triplicates of the same sediment sample were conducted). The bottles were hermetically sealed for > 1 month and periodically shaken. The ^{222}Rn concentration in water was measured using the RAD7 coupled to the gas extraction accessory for bottles and corrected to the specific ratio of pore water/solids in sediments following Stieglitz et al. (2013).

Surface and pore waters

Between 0.5 and 2 liters of pore water was collected for Ra analysis via vacuum hand pump into plastic containers, for all sampling dates. The plastic containers were left for several hours (or overnight) to allow particles to settle to the bottom of the container. Afterward, the water overlying the particles was decanted off into a graduated cylinder and volume was recorded; this water was then filtered through raw acrylic fiber (Mn-free) to further remove any particles. In the laboratory, hypoxic (DO < 3 mg L^{-1}) pore-water samples were aerated for ~ 20 min; after aeration, Mn-fibers were added directly to the water sample and periodically stirred (< 1 h) to quantitatively adsorb all Ra from the solution. Two water samples were subjected to a second Mn-fiber addition; these second fibers did not produce any counts (above background) and thus we assume a 100% initial Ra yield. Large volume (> 10 liters) endmember samples were traditionally filtered through cartridges (< 1 L min^{-1}). Mn-fibers were triple rinsed, partially dried (Sun and Torgersen 1998*a*), and counted using a RaDeCC to measure the short-lived ^{224}Ra isotope; samples were counted again 1 week after collection to determine ^{223}Ra (Moore and Arnold 1996). Mn-fibers were recounted approximately 3 weeks after sample collection to measure ^{228}Th, to calculate excess ^{224}Ra (hereafter denoted $^{224}Ra_{ex}$). Detector efficiencies were determined using a ^{232}Th and ^{227}Ac standard; analytical counting uncertainties were calculated by standard rules of error propagation and the results were decay corrected back to the sample collection time (Garcia-Solsona et al. 2008).

For ^{222}Rn analysis, pore waters from May, June, and November were collected into 250-mL air-tight bottles, which were coupled to the piezometer tubing to minimize water–air contact, via vacuum hand pump. Lagoon and Mediterranean Sea endmembers were collected in 2 L air-tight bottles using a small submersible pump and submerging the bottle beneath the water surface to minimize gas loss. ^{222}Rn samples were analyzed using the radon-in-air monitor RAD7 coupled to a gas extraction accessory for bottles (Durridge) and decay corrected back to the sample collection time; uncertainties are presented as ± 1 SD.

Water samples for solute and carbon measurement were syringe filtered using 0.45 μm cellulose acetate filters into rinsed 60 mL low-density polyethylene vials. Water samples were diluted 10x with deionized water and analyzed for dissolved Ba and Si by inductively coupled plasma - optical emission spectrometry (Horiba Jobin Yvon Ultima2®); analytical precision is ≤ 10%. DIC and dissolved organic carbon (DOC) were analyzed using a Shimadzu®, and results are expressed in molar quantities of carbon; analytical precision is ≤ 5%.

Ancillary parameters

To investigate the driving mechanisms of seawater circulation through swash-zone, we obtained (1) hourly wind data (speed and direction) from the nearby meteorological station "Leucate" from Météo France, the French meteorological service, and (2) wave sensor data (half-hour intervals) from the nearby buoy "Leucate" (ID 01101) from CEREMA. Wind and waves contribute to local sea levels and lead to a dynamic interaction between seawater and pore waters. In this study, we separate total water levels at the coast into wind and wave contributions as, respectively, wind-driven setup and wave run-up at the beach. The wind setup formulation (S_{wind}; Dean and Dalrymple 2004) relates measured wind speeds, direction relative to the shore-normal and distance over which the wind blows (fetch) to a local increase in water levels (Eq. 2) presuming that the wind is present for a long enough time to reach an equilibrium state.

$$S_{wind} = h^* \left(\sqrt{1 + \frac{A_s x}{L}} - 1 \right) \quad (2)$$

In which, A_s is

$$A_s = \frac{2n\tau_s L}{\rho_w g h^2} \quad (3)$$

where

$$\tau_s = \rho_w c_t W^2 \quad (4)$$

In Eqs. 2–4, h is the mean water depth over the fetch length L, x is the position along the fetch (in this case, $x = L$ as we are at the coast), and A_s is a dimensionless parameter containing n, in which $n = 1 - (\tau_b/\tau_s)$ to account for bottom (τ_b) and wind shear stress (τ_s). Here, n is set as 1.15, ρ_w represents water density, g is the gravitational acceleration, c_t is a friction coefficient, and W is the wind speed (shore-normal), usually measured at 10 m elevation.

The wave contribution to total sea level at the coast is calculated using a statistical bulk run-up formula (Stockdon et al., 2006). Stockdon et al. (2006) relates offshore measured wave conditions such as significant wave height relative to the

Table 1. Bulk solid-phase radionuclide activities and measured distribution coefficients (K_D) for a salinity of 27 and 38

ID	Distance from sea (m)	^{226}Ra (dpm g^{-1})	^{228}Ra (dpm g^{-1})	^{228}Th (dpm g^{-1})	^{228}Th/^{226}Ra	K_D (S = 27; cm^3 g^{-1})	K_D (S = 38; cm^3 g^{-1})
5-PW3-A	23	0.57 ± 0.02	0.66 ± 0.04	0.67 ± 0.01	1.17 ± 0.04	—	—
5-2-PW3-A	44	0.58 ± 0.04	0.41 ± 0.07	0.79 ± 0.07	1.37 ± 0.15	3.1	2.1
5-PW5-A	43	0.58 ± 0.02	0.47 ± 0.03	0.61 ± 0.02	1.05 ± 0.05	2.4	1.4
5-PW7-A	63	0.50 ± 0.02	0.55 ± 0.04	0.56 ± 0.01	1.12 ± 0.05	—	—

shore-normal and peak period to a statistical value for wave run-up (R_{wave}) at the beach (2% exceedance) following:

$$R_{wave} = 1.1\left(0.35\beta_f\sqrt{H_0L_0} + \frac{\sqrt{H_0L_0\left(0.563\beta_f^2 + 0.004\right)}}{2}\right) \quad (5)$$

wherein β_f is the beach face slope, H_0 is the offshore wave height (shore-normal), and L_0 represents the offshore wave length. The superposition of the wind and wave contribution results in a time-varying total water level.

The physical impact of wind and waves on seawater circulation in the swash-zone might be far from instantaneous; for example, a certain adaptation time or lag may exist between seawater circulation and the occurring wind and wave conditions. To investigate the importance of this adaptation time lag, mean wind and wave data variables were binned into seven different time intervals: 2 weeks, 1 week, 72 h, 48 h, 24 h, 12 h, and 6 h prior to each sampling. These time intervals were chosen to represent the range in time-scale that is traced by short-lived ^{222}Rn, ^{223}Ra, and ^{224}Ra$_{ex}$. Binned averages for different wind and wave parameters were compared to radionuclide-derived advection velocities (*see* Discussion section) to investigate any potential temporal variability caused by wind setup and wave setup. Multiple linear regression analysis for uncorrelated variables was performed using XLSTAT 2018.

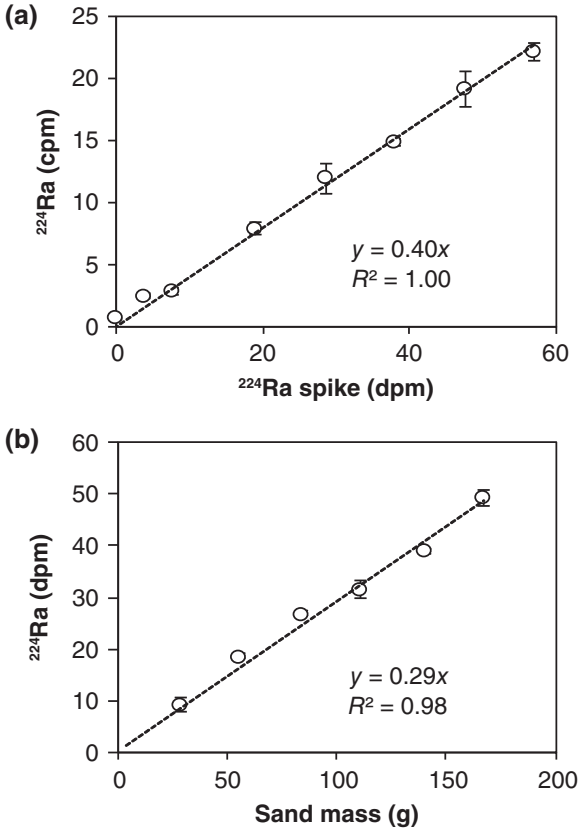

Fig. 2. Sediment counting efficiency of the RaDeCC system determined from a ^{224}Ra standard addition spike, where the counting efficiency is equal to the slope of the cpm vs. dpm linear regression (**a**). ^{224}Ra sediment activity as a function of sample load (**b**). Note that the error bars are generally smaller than the symbol size.

Results

Sediment

Total (surficial and lattice-bound) ^{226}Ra (0.50–0.58 dpm g^{-1}), ^{228}Ra (0.41–0.66 dpm g^{-1}), ^{228}Th (0.56–0.79 dpm g^{-1}), and sediment porosity (0.38 ± 0.1) showed little variability across the beach transect (Table 1). RaDeCC detectors exhibited a linear increase in ^{224}Ra cpm with increasing ^{224}Ra added (solution spike and sediment mass), suggesting that the RaDeCC is suitable for measuring the surface-exchangeable Ra of beach sands (Fig. 2). Surface-exchangeable Ra was similar between sediment samples, with a mean (± STD; four replicate measurements) activity of 0.0025 ± 0.0002 dpm g^{-1} (n = 4) for ^{223}Ra and 0.041 ± 0.006 dpm g^{-1} (n = 4) for ^{224}Ra (Table 2). Thus, as compared to the bulk ^{228}Th, the recoil efficiency of ^{224}Ra into pore fluid was between ~ 5% and 7%, as expected for coarse-grained sands (Copenhaver et al. 1993; Porcelli 2008). We assume that all ^{222}Rn input is similar across the beach transect, as evidenced by the solid-phase ^{226}Ra distribution (Table 1). The production rate (P; dpm cm^{-3}) of Ra was estimated as

$$P = \frac{(1-\varphi)}{\varphi} * \rho_{sed} * Ra_{surf} \quad (6)$$

where φ is the sediment porosity (0.38), ρ_{sed} is the grain density (2.65 g cm^{-3}), and Ra_{surf} is the activity of surface-exchangeable Ra (dpm g^{-1}). For the beach transect samples, the production rate (P) with zero partitioning is equal to

Table 2. Sediment surface-exchangeable ^{223}Ra and ^{224}Ra activities, determined via RaDeCC

ID	Distance from sea (m)	^{223}Ra (dpm g^{-1})	^{224}Ra (dpm g^{-1})	^{224}Ra/^{223}Ra
5-PW3-A	23	0.0022 ± 0.0003	0.034 ± 0.001	15.7
5-PW5-A	43	0.0025 ± 0.0005	0.038 ± 0.002	15.2
5-PW6-A	53	0.0024 ± 0.0005	0.050 ± 0.002	20.9
5-PW7-A	63	0.0028 ± 0.0003	0.041 ± 0.001	15.0
AVG ± STD		0.0025 ± 0.002	0.041 ± 0.006	16.7 ± 2.4

Table 3. Sediment equilibration results. Total ^{224}Ra/^{222}Rn activity ratios consider a mean surface-exchangeable ^{224}Ra activity of 0.041 ± 0.006 dpm g^{-1} (176 ± 25 dpm L^{-1})

	^{222}Rn* (dpm L^{-1})	^{223}Ra (dpm L^{-1})	^{224}Ra (dpm L^{-1})	^{224}Ra/^{222}Rn	
				Dissolved	Total
Salinity 27	160 ± 20	2.5 ± 0.3	29.0 ± 3.0	0.18 ± 0.03	1.28 ± 0.22
Salinity 38	160 ± 20	3.0 ± 0.2	52.5 ± 4.0	0.33 ± 0.05	1.43 ± 0.24

*^{222}Rn equilibration results are only for a salinity of 38 but assumed to be representative for all salinities (minor influence of water salinity on ^{222}Rn partitioning).

10.6 ± 1.0 dpm L^{-1} for ^{223}Ra and 176 ± 25 dpm L^{-1} for ^{224}Ra. The resulting theoretical dissolved equilibrium ^{224}Ra/^{223}Ra activity ratio is thus 16.6 ± 2.8 and is likely not varying across the beach transect (Table 2). Note that the difference between the above activities (P) and the actual rate of Ra production (dpm L^{-1} d^{-1}) is simply a function of the Ra isotope decay constant (λ).

Mean K_D values equal 1.7 ± 0.9 cm^3 g^{-1} at a salinity of 38 (Mediterranean seawater) and 2.7 ± 0.7 cm^3 g^{-1} at a salinity of 27 (average of two sediment samples; Table 1). Considering sediment porosity and grain density, K is equal to 7.5 ± 3.9 at a salinity of 38 and 11.6 ± 3.0 at a salinity of 27 [$K = K_D \times \{(1 - \varphi) \times \rho_{sed}/\varphi\}$]. An estimate can be made of the magnitudes of the pore-water ^{226}Ra and adsorbed ^{226}Ra included with the sediments based on the determined K_D values (1.7–2.7). For a porosity of 0.38, there was 0.23 $cm^3_{water}/g_{dry\ sediment}$. The experiments used 11–20 g of sediment, and the pore-water ^{226}Ra in the beach sand was measured as 74 dpm 100 L^{-1}. Pore-water ^{226}Ra that would have been present in the two sediment aliquots at the start of the sorption experiments would have been 0.002 and 0.003 dpm, respectively. The in situ adsorbed ^{226}Ra would have thus been 0.019 and 0.024 dpm for the 11 and 20 g experiments, respectively. Thus, the total ^{226}Ra contributed from dissolved and adsorbed fractions at the start of the experiment was 0.02–0.03 dpm. These are small fractions of the total ^{226}Ra activity of the solid phase determined by gamma spectrometry before the K_D experiments (0.5–0.6 dpm g^{-1}, or ~ 6–12 dpm total contributed by the 11–20 g aliquots) and, as noted above, would have been included in the "starting" ^{226}Ra used to calculate K_D after the sorption experiments (Table 1). We also note that the natural "adsorbed" ^{226}Ra would have contributed at most 10% of the sorbed Ra at the conclusion of the K_D experiment, and thus no correction was made for it in calculating K_D. The K_D values measured here (1.7–2.7) are comparable to that determined for beach sand by Colbert and Hammond (2008) (K_D = 1.6) and Beck and Cochran (2013) (K_D = 1.14–1.60), using a different method.

Sediment incubation experiments represent an equilibrium Ra activity in pore water (production = decay) controlled by the ionic strength of the solution (via K) and may additionally include inputs of Ra from sediment dissolution (i.e., weathering). The equilibrium pore-water ^{223}Ra activity was equal to 2.5 ± 0.3 and 3.0 ± 0.2 dpm L^{-1} for a salinity of 27 and 38, respectively; equilibrium $^{224}Ra_{ex}$ activity was equal to 29.0 ± 3.0 and 52.5 ± 4.0 dpm L^{-1} over the same salinity interval, and the resulting ^{224}Ra/^{223}Ra ratios are thus 11.6 ± 1.8 and 17.5 ± 1.8 for salinities of 27 and 38, respectively (Table 3). Pore-water ^{222}Rn activity in equilibrium with sediments was 160 ± 20 dpm L^{-1} (average of three samples).

Changes in salinity (ionic strength) drive changes in the partitioning (K) of Ra between dissolved and solid phases (Webster et al. 1995; Gonneea et al. 2008). The activity ratio of mobile ^{224}Ra/^{222}Rn is approximately equivalent to the ratio of the emanation efficiency of ^{222}Rn and the recoil efficiency of ^{224}Ra in fresh groundwater systems when steady-state is achieved (Porcelli and Swarzenski 2003), under the assumption that all alpha-decay radionuclides are supplied at similar rates to that of ^{222}Rn (Krishnaswami et al. 1982). ^{222}Rn is an inert, noble gas whose distribution in pore fluid is supplied chiefly by alpha recoil from sediment surfaces, thus ^{222}Rn is not partitioned between solid and dissolved phases

like Ra. Bulk solid-phase $^{228}Th/^{226}Ra$ activity ratios, the parent isotopes of $^{224}Ra/^{222}Rn$, are between 1.05 and 1.37 (Table 1); therefore, pore waters in equilibrium with sediment surfaces should have $^{224}Ra/^{222}Rn$ activity ratios within this range if there is no partitioning of Ra between sediment surfaces and solution. Pore-water $^{224}Ra/^{222}Rn$ activity ratios determined from the equilibration experiments are between 0.18 ± 0.03 for a salinity of 27 and 0.33 ± 0.05 for a salinity of 38 (Table 3). Assuming that all ^{222}Rn is input at a constant rate and considering a mean surface-exchangeable ^{224}Ra activity of 0.041 ± 0.006 dpm g^{-1} (176 ± 25 dpm L^{-1}), then the total (dissolved + surface-bound) $^{224}Ra/^{222}Rn$ activity ratio is 1.28 ± 0.22 for a salinity of 27 and 1.43 ± 0.24 for a salinity of 38 (Table 3), approximately within the range of the bulk $^{228}Th/^{226}Ra$ activity ratios.

General water parameters

Precipitation largely occurs during fall and spring months, with little rainfall during the 6-month sampling interval (May–November 2017; Fig. 3). Total precipitation for the week prior to each sampling event equaled 3.4, 0.0, 0.2, 0.2, 2.4, and 0.8 mm for May, June, July, August, September, and November, respectively. Wind speed and direction are dominated by two modes, blowing predominantly from either the sea (~ 90°) toward land or from land (~ 315°) toward the sea (Fig. 3). Significant wave height and direction follow a similar pattern to that of wind speed (Fig. 3).

Lagoon surface water salinity increased between May and September 2017 from 26 to 52 due to low precipitation and high temperatures (Fig. 4). In May, pore waters sampled between the lagoon and Mediterranean Sea primarily reflected the salinity of the lagoon endmember (26). Pore waters with a slightly lower salinity (~ 24) were likely derived from past lagoon conditions (April or earlier). During the spring, lagoon water levels were at a maximum (Table 4), and the May sampling period therefore experienced the greatest hydraulic gradient between the lagoon and sea, further evidenced by the second transect (T2), sampled over 250 m away (Fig. 4).

In June and July, pore waters sampled closest to the lagoon were similar in salinity as the lagoon endmember (Fig. 4). During this time period, pore-water salinities decreased continuously with increasing distance from the lagoon toward the sea, reflecting a mixture between recent infiltration of the actual lagoon endmember and older low-salinity (~ 24) lagoon waters. During August and September, pore waters sampled next to the lagoon were significantly lower in salinity than the lagoon endmember (33 vs. 45 on 30 August 30; 33 vs. 52 on 25 September). High evaporation rates and low precipitation during August and September (Fig. 3) resulted in a diminished hydraulic gradient between the lagoon and the sea, corresponding to a period in which lagoon surface water levels were relatively low (Table 4). Consequently, the high-salinity lagoon waters did not penetrate into the sand barrier during that period, resulting in a large contrast in salinity between the lagoon waters and the pore waters close to the lagoon. In November, strong winds created an opening in the beach spit, forming a natural outlet to the sea, where the barrier beach was approximately half of the width (~ 40 m) that it had been in previous months. Because of the input of seawater (salinity = 38) into the lagoon, the salinity of the lagoon waters decreased to reach a salinity of 39 (in comparison to 52 in September).

Radionuclide distribution

Pore waters sampled directly adjacent to the lagoon (1–3 m) in May, June, and July, which were similar in salinity to that of the lagoon (Fig. 4), have elevated ^{222}Rn, ^{223}Ra, and $^{224}Ra_{ex}$ over the lagoon. This pattern indicates relatively recent lagoon water infiltration and subsequent radionuclide ingrowth from contact with the sediment (Figs. 5–6). ^{222}Rn, ^{223}Ra and $^{224}Ra_{ex}$ activities reach maximum activities within a ~ 30 m distance from the lagoon. Within the first ~ 5–15 m of the Mediterranean shoreline, pore-water salinities reflected that of the Mediterranean Sea (~ 38), representing a zone in which the beach face was exposed to constant wave setup. ^{222}Rn, ^{223}Ra and $^{224}Ra_{ex}$ increased with increasing distance from the shoreline in this seawater salinity zone (Fig. 5). Vertical profiles show generally increasing activities of pore-water ^{222}Rn, ^{223}Ra and $^{224}Ra_{ex}$ with increasing depth, near both the lagoon and the sea (Fig. 7).

In situ pore-water $^{224}Ra/^{222}Rn$ activity ratios were between 0.2 and 0.4 in samples taken in the center of the beach transect (n = 14), which are assumed to be in equilibrium with sediment surfaces, as pore-water $^{224}Ra/^{222}Rn$ activity ratios determined from the sediment equilibration experiments were 0.18–0.33. Considering a mean surface-bound ^{224}Ra activity (0.041 ± 0.006 dpm g^{-1}; Table 2) and assuming that all labile ^{222}Rn is in solution, then the total (dissolved + surface-bound) in situ $^{224}Ra/^{222}Rn$ activity ratio is equal to 2.2 ± 0.7 (n = 14). It is important to note that we do not consider ^{222}Rn produced from dissolved ^{226}Ra and any potential absolute differences in the $^{238}U/^{232}Th$ activity ratio of the sediment (Luo et al. 2000).

Dissolved solutes

DOC was depleted by ~ 0.1–0.4 mmol L^{-1} in beach pore waters, with respect to theoretical, two-endmember linear mixing between lagoon surface and Mediterranean Sea endmembers (depending upon position and season; Fig. 8). Pore-water DIC was enriched over both surface endmembers, increasing in concentration toward the center of the beach (Fig. 8). There was more DIC observed than expected from DOC consumption (~ 2–3 mmol L^{-1}), suggesting that there was DIC input to the pore waters from the weathering of carbonate minerals. Consumption of particulate organic carbon (if present in the sand barrier) may also contribute to the DIC enrichment in pore waters. DSi transects were similar to DIC, reaching a relative maximum (100 μmol L^{-1} in August) in the center of the beach (Fig. 8), indicating that dissolution of Si minerals takes place within the sand barrier and releases DSi

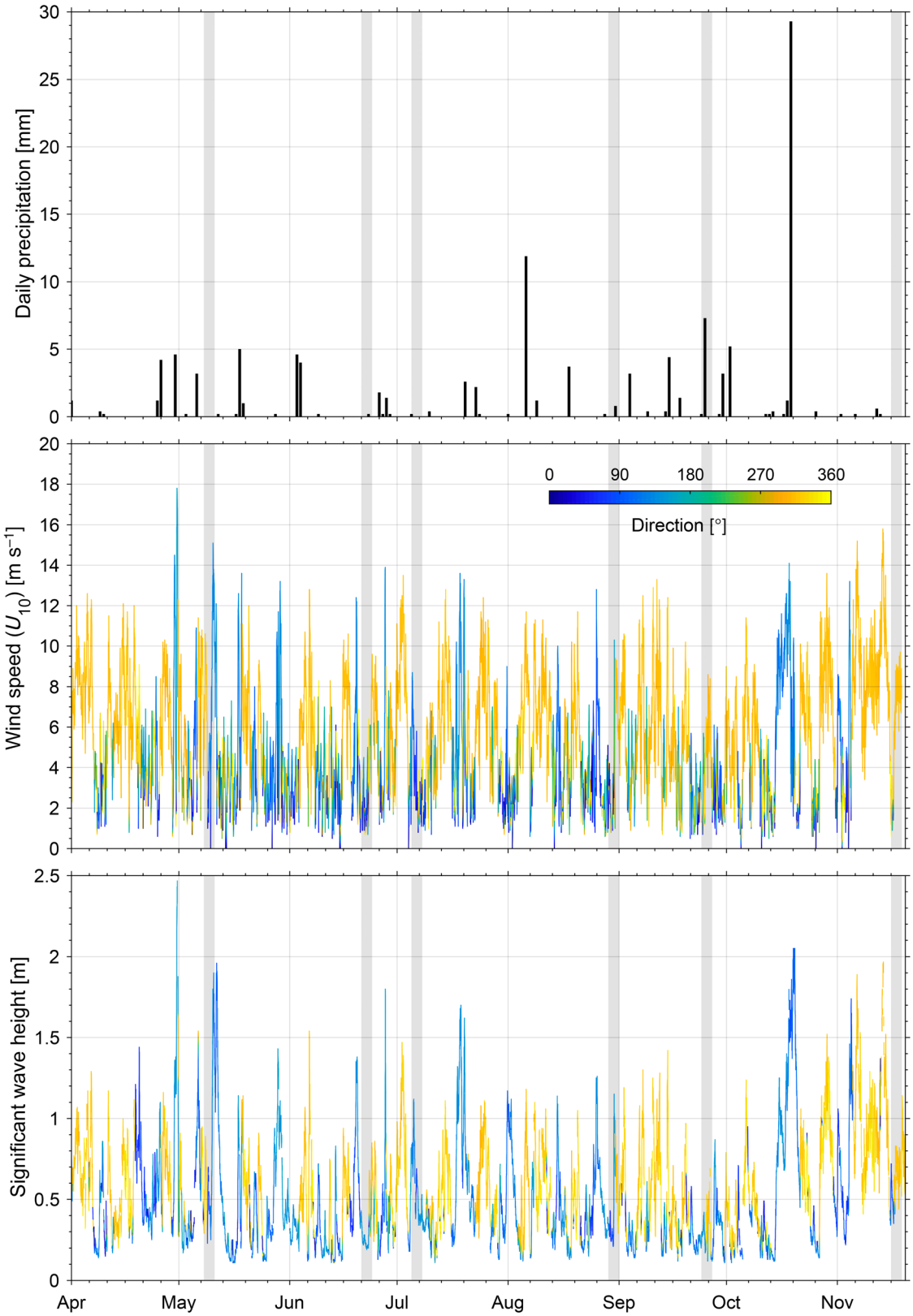

Fig. 3. Precipitation, wind speed, and wave height during 2017. Wind and wave direction are plotted by color. Wind speed data are from "Meteo France," and wave height data are from CEREMA. Sampling periods are indicated by vertical gray lines. The dominant winds in the region include wind from the NW (i.e., "Tramontane," ~ 315°, yellow color on the plot) and wind from the sea (E; ~ 90°, blue color on the plot).

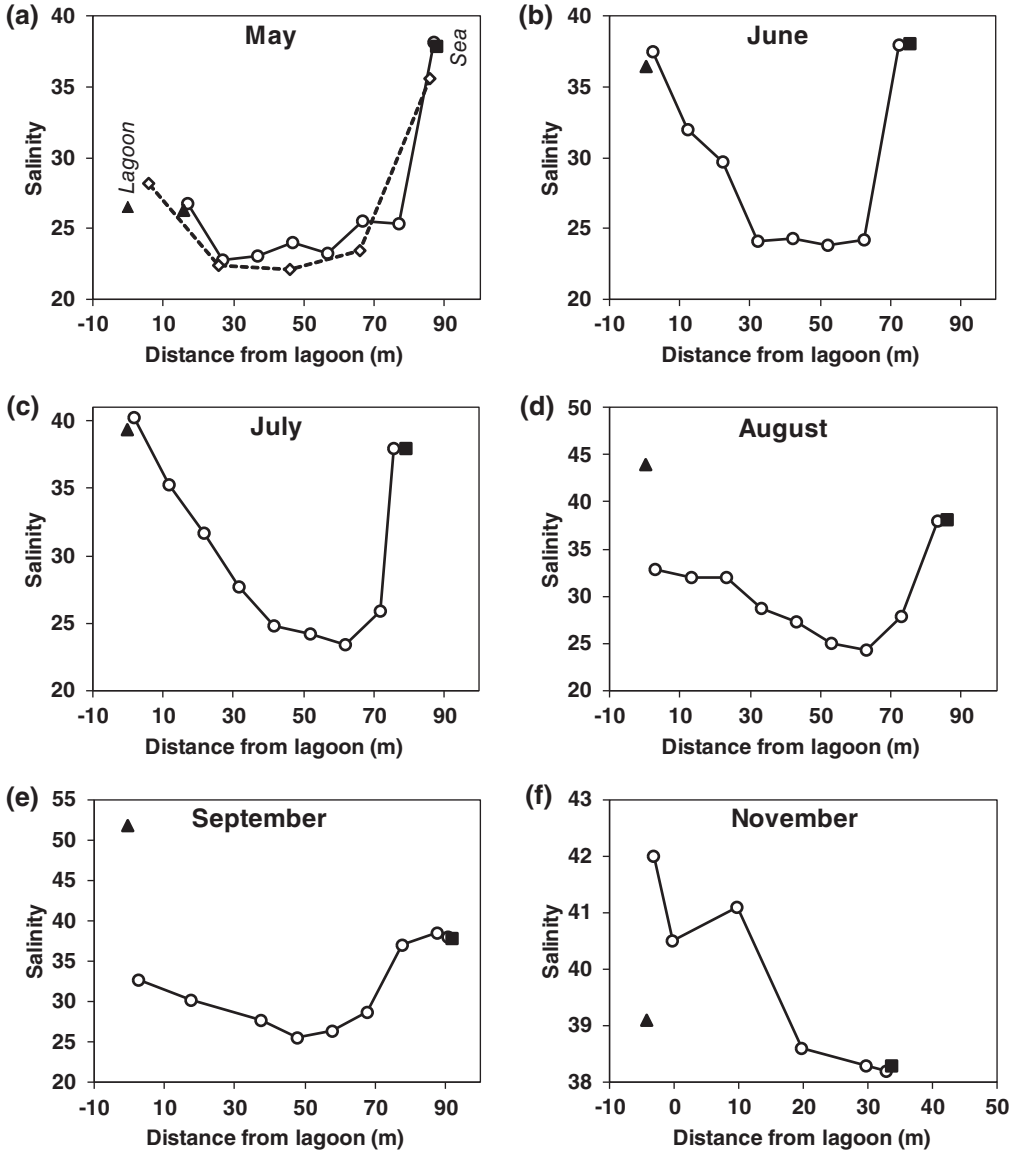

Fig. 4. Spatial distribution of shallow pore-water salinity (50 cm depth; hollow circles) with respect to lagoon surface water (filled triangle) and Mediterranean Sea (filled square) endmembers for May (a), June (b), July (c), August (d), September (e) and November (f) 2017. During May, a second transect (Transect 2) was sampled and is depicted by diamonds connected with a dashed line; note T1 is offset during May for clarity. Note the *y*- and *x*-axes differ between plots.

into the pore water (Anschutz et al. 2009; Tamborski et al. 2018). Vertical DIC and DSi profiles sampled closest to the Mediterranean Sea increased in concentration with increasing depth, similar to ^{222}Rn and ^{223,224}Ra, for all six sampling seasons (Fig. 7). Pore waters at 50 cm depth were enriched over surface water concentrations between 25 and 110 μmol L^{-1} for DIC and between 4 and 11 μmol L^{-1} for DSi. Transects of dissolved Ba, a chemical analog to Ra, primarily followed two-endmember mixing between surface water endmembers (Fig. 8), whereas vertical profiles taken near the sea were relatively constant in concentration with depth (Fig. 7). Therefore, these profiles suggest that pore-water Ra distributions were significantly impacted by ingrowth from water-sediment interaction (Fig. 5). All surface and pore-water data are summarized in the Supporting Information.

Discussion

Reactive-transport model

Theory

The change in Ra isotope activity with time may be described with a 1-D reactive-transport model. Here, we use a horizontal reactive-transport model to describe the Ra activity of the beach transects as a function of advective lagoon–sea water exchange. In parallel, we use a vertical reactive-transport model to describe the Ra activity of the profiles taken adjacent

Table 4. Lagoon surface-water elevation and water table elevation above sea level. Water table elevation measurements are taken closest to the lagoon edge, approximately 73 m from the Mediterranean Sea, and are corrected for the elevation of the beach surface (measured during June). November is not included. Lagoon surface-water elevation data are from the Parc Naturel Régional de la Narbonnaise en Méditerranée monitoring station Coussoules (Fig. 1)

	Surface water elevation (m)	Water table elevation (m)
May	0.85	0.36
Jun	0.75	0.29
Jul	0.60	0.24
Aug	0.53	0.19
Sep	0.45	0.13
Nov	0.55	—

to the Mediterranean Sea, as a function of seawater circulation. Neglecting hydrodynamic dispersion and assuming steady-state conditions (Krest and Harvey 2003; Michael et al. 2011), the advection of Ra in pore water can be described as:

$$A(x) = \frac{P}{1+K} + \left(A_o - \frac{P}{1+K}\right) * e^{-\Delta x \lambda v^{-1}} \quad (7)$$

where $A(x)$ is the Ra activity (dpm L^{-1}) at distance x (m) from a defined boundary condition, A_o is the initial Ra activity at a $x = 0$, P is the Ra isotope production rate (dpm L^{-1}), K is the dimensionless Ra partition coefficient (adsorbed exchangeable Ra on the solid/dissolved Ra), λ is the Ra isotope decay constant (d^{-1}), and v is the advective pore-water velocity (m d^{-1}). Under homogeneous conditions in which groundwater salinity is constant and the initial Ra concentration is zero, Kiro et al. (2012) note that Eq. 7 may be further reduced if $x > \frac{vt}{1+K}$ (where t is time) to:

$$A(x) = \frac{P}{1+K} * \left(1 - e^{-\Delta x \lambda v^{-1}}\right) \quad (8)$$

Considering $^{224}Ra_{ex}/^{223}Ra$ activity ratios, the solution to Eq. 7 becomes:

$$\frac{^{224}Ra}{^{223}Ra} = \frac{\frac{P_{224}}{1+K} + \left(A_{224^o} - \frac{P_{224}}{1+K}\right) * e^{-\Delta x \lambda_{224} v^{-1}}}{\frac{P_{223}}{1+K} + \left(A_{223^o} - \frac{P_{223}}{1+K}\right) * e^{-\Delta x \lambda_{223} v^{-1}}} \quad (9)$$

Equations 7–9 may be modeled using a numerical curve-fitting approach, by adjusting the advective velocity term (v) to minimize the root-mean-square error of the model with respect to the observed data. We have explicitly measured A_o, P (Table 2), and K (via K_D and $^{224}Ra/^{222}Rn$ activity ratios; Tables 1, 3) to be used in the model calculations.

$^{224}Ra_{ex}/^{223}Ra$ activity ratios were chosen to model the horizontal advection of lagoon–sea water exchange (Eq. 9). Small-scale sediment heterogeneity may result in variable (equilibrium) pore-water ^{223}Ra and ^{224}Ra activity distributions over the ~ 100-m long beach transects (Fig. 5). Sediment-exchangeable $^{224}Ra/^{223}Ra$ activity ratios were relatively constant across the beach transect, indicating a homogeneous sediment distribution (Table 2); therefore, $^{224}Ra/^{223}Ra$ activity ratios are better suited to identify disequilibrium between pore waters and sediment surfaces (Eq. 9) over absolute activities (Eq. 7 and 8) at such a spatial scale. Here, the horizontal boundary condition is set as the lagoon surface water endmember for May–July, to represent lateral flow through the barrier beach, driven by a positive hydraulic gradient between the lagoon and the sea (Table 4). We cannot assume steady-state conditions for August–September (because of the diminished hydraulic gradient) and November (the spit was recently breached); therefore, we do not model these months. The horizontal model is limited to shallow pore-water samples only, where we could collect sediment samples. Shallow pore-water samples closest to the lagoon are lower in ^{223}Ra and $^{224}Ra_{ex}$ activity compared to deeper samples (Fig. 7); therefore, we consider these shallow samples as representative of this active water exchange zone, here defined as 1.0 m depth.

To estimate seawater circulation in the swash-zone, radionuclide activities were modeled for the pore-water profiles sampled closest to the Mediterranean Sea (A_o) (Eq. 7), where pore-water salinities were equivalent to seawater (Fig. 7). The vertical advective velocity is a rate of flushing exchange (net zero water flux), in which Ra atoms are lost from pore waters, similar to pore-water exchange creating a (total) ^{224}Ra deficit relative to its surface-bound parent ^{228}Th (Cai et al. 2014), but here we only consider the dissolved Ra pool. The short-lived radionuclide flux is not necessarily driven by a net water (discharge or recharge) flux; rather, the Ra flux can be sustained by seawater circulation (net zero water flux; Cook et al. 2018*a*). The deficit of short-lived ^{222}Rn, ^{223}Ra, and $^{224}Ra_{ex}$ does not reflect instantaneous seawater circulation for the exact time of sampling; rather, the radionuclide deficit is integrating across the time-scale of radionuclide ingrowth and decay. $^{224}Ra_{ex}/^{223}Ra$ activity ratios were not used for the vertical model because the range of the $^{224}Ra/^{223}Ra$ activity ratios (and its relative uncertainty) was much lower compared to the larger range in activity ratio observed for the horizontal transects (~ 10–35). Terms used in the 1-D horizontal and vertical reactive transport models are summarized in Table 5.

Sensitivity and assumptions

Reactive-transport model sensitivity to changes in production rate (P) and Ra partition coefficient (K; or the "retardation factor" $R = 1 + K$) have been summarized in detail elsewhere (Tricca et al. 2001; Krest and Harvey 2003; Michael et al. 2011; Kiro et al. 2015; Tamborski et al. 2017). Michael et al. (2011) note that the ratio of Ra production to retardation is difficult to quantify and should be done so carefully in order to use the 1-D reactive-transport model in any quantitative, meaningful way. Tamborski et al. (2017) showed that radionuclide-derived pore-water residence times ($\tau = v/d$) within tidal beach

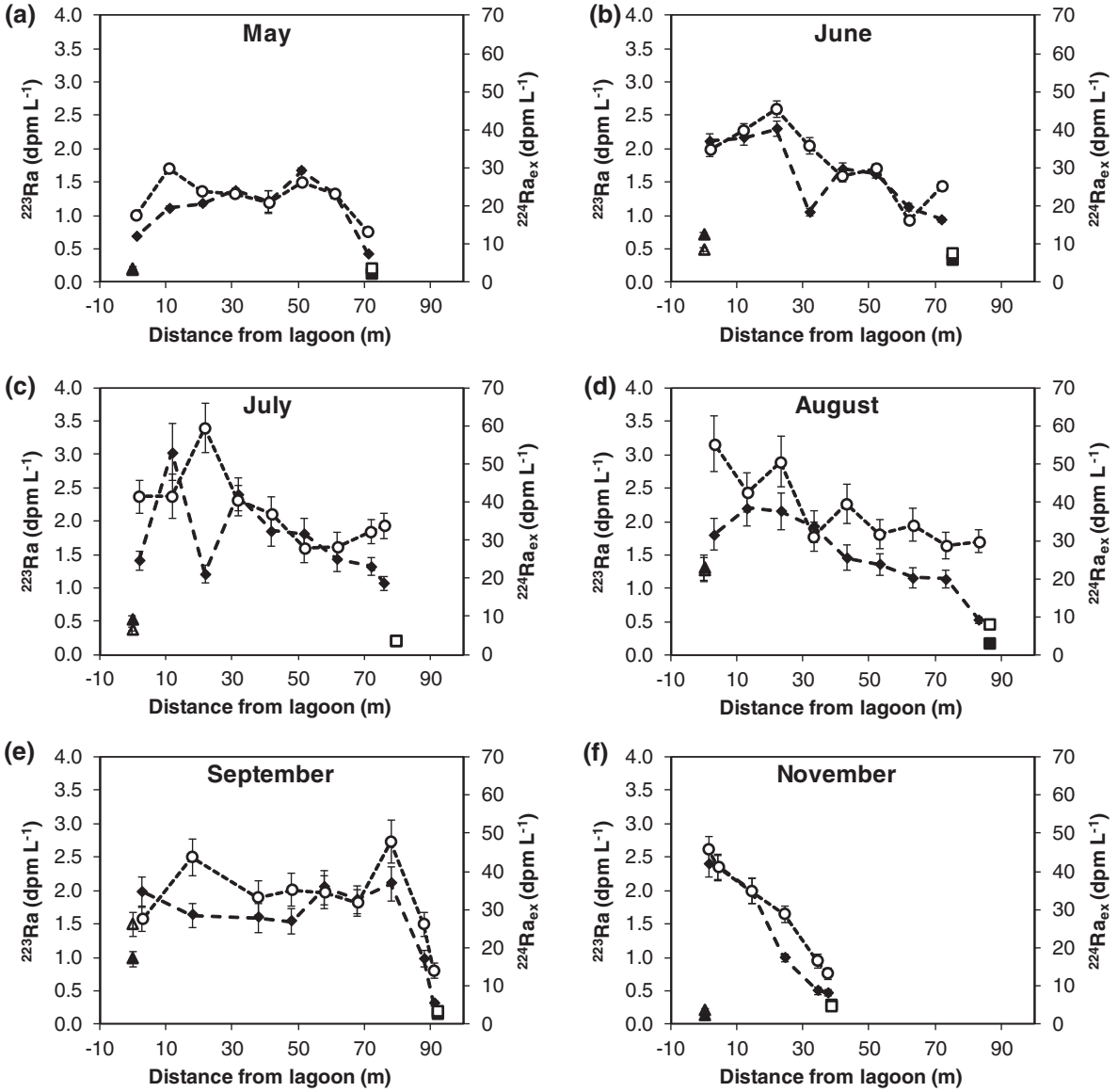

Fig. 5. Spatial distribution of shallow (50 cm depth) pore-water ^{223}Ra (filled diamonds) and ^{224}Ra$_{ex}$ (hollow circles) with respect to lagoon surface water (triangle) and Mediterranean Sea (square) endmembers for May (a), June (b), July (c), August (d), September (e) and November (f) 2017.

environments are sensitive to values of P for long residence times, but less sensitive when residence times are low (approximately less than 1 d). It is important to note that flow velocity is spatially and temporally variable and is not as simple as the depiction of the 1-D model due to subsurface heterogeneity (Michael et al. 2011).

Sediment equilibration-derived K values (from ^{224}Ra/^{222}Rn; Table 3) for two different salinity solutions (27 and 38) were not significantly different when considering surface-bound ^{224}Ra, with respect to their range in uncertainties. In situ determined K values (2.2 ± 0.7) were slightly higher than those determined from the sediment equilibration experiments and exhibited greater variability, as evidenced by a large standard deviation. All K values estimated from ^{224}Ra/^{222}Rn activity ratios are lower than experimentally determined values from the sorption experiments (7.5–11.6). This discrepancy may be explained by an experimental particle concentration effect, as observed for the highly particle-reactive ^{234}Th (Honeyman et al. 1988). In theory, K_D should remain constant regardless of the particle-to-solution ratio used experimentally; in practice, measured K_D values are greater for experiments with smaller particle-to-solution ratios, which can result in a factor of ~ 10 difference in K_D (Honeyman et al. 1988). In situ particle-to-solution ratios are an order of magnitude greater than particle-to-solution ratios typically used for K_D experiments. Indeed, Cochran et al. (1986) determined that the K_D for Th was ~ 10^5 cm^3 g^{-1} in nearshore (Buzzards Bay, Massachusetts) sediment pore waters, in contrast to values two

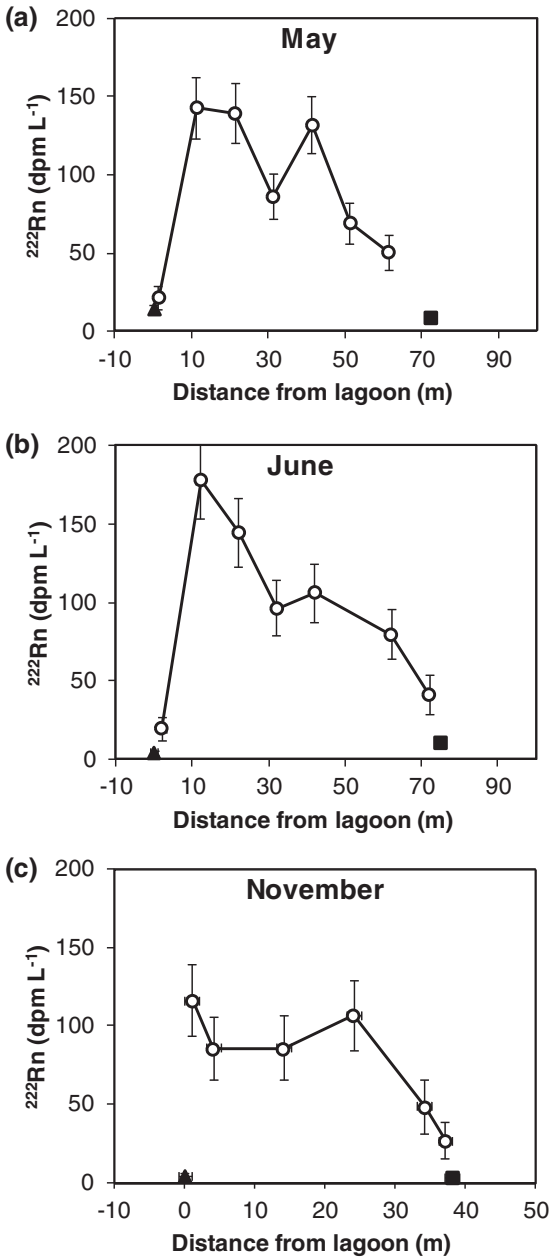

Fig. 6. Spatial distribution of shallow pore-water (50 cm depth; hollow circles) ^{222}Rn with respect to lagoon surface water (filled triangle) and Mediterranean Sea (filled square) endmembers. ^{222}Rn was only sampled during May (a), June (b), and November (c). Note the *x*-axes differ between plots.

orders of magnitude greater (~ 10^7 cm^3 g^{-1}) in the deep sea (Bacon and Anderson 1982; Honeyman et al. 1988).

Considering the range in K values noted above, we elect to use values derived from in situ ^{224}Ra/^{222}Rn activity ratios for samples assumed to be in equilibrium with sediment surfaces, taken in the center of the beach transect (2.2 ± 0.7; n = 14). We use a range in K determined from the standard deviation to represent a minimum K (1.5) for salinity 38 and a maximum K (2.9) for salinity 27. This range in K is qualitatively validated from the sorption K_D experiments (despite the particle-concentration effect noted above), which provides additional confidence to this approach. The uncertainty of the sediment equilibration K values prevents us from accurately distinguishing between salinities of 27 and 38, despite observable differences in experimental (Table 3) and in situ (Fig. 5) dissolved ^{223,224}Ra activities.

Ra desorption from estuarine sediments is a nonlinear process chiefly governed by the availability of Ra on particle surfaces and the major ion present in solution, where nonlinearity is typically greatest between a salinity of 0 and ~ 15 (Webster et al. 1995). Changes between K and salinity for relatively high ionic strength solutions (i.e., > 30% seawater composition for seawater salinity of 36) may be approximated as linear (Webster et al. 1995; Kiro et al. 2012, 2013). Here, we assume a linear relationship between K and salinity along the horizontal groundwater flow path for salinity 27 (K = 2.9) and salinity 38 (K = 1.5), based on the observed pore-water salinity distribution (Fig. 4). We further extrapolate to a salinity of 22 and 42 to match the observed minimum and maximum salinity. Bulk ^{228}Th (Table 1) and surface-exchangeable ^{224}Ra (Table 2) are relatively uniform throughout the beach. We assume that the mean value of P is representative of the beach transect in the horizontal direction. Values of P were measured for surficial sediments (~ 0–50 cm depth) along the investigated transect; values of P may change with depth in the vertical model due to differing amounts of ^{228}Th present on sediment surfaces. Spatially variable Ra and Rn production can occur if there are significant differences in the Fe and Mn (hydr)oxide coatings on sediment surfaces (Dulaiova et al. 2008; Beck and Cochran 2013) or barite ($BaSO_4$) precipitation (Kiro et al. 2012), which we do not consider at present. For the vertical reactive-transport model, the term $[P/(1 + K)]$ is simply constrained from the sediment incubation experiments for seawater salinity (Table 3).

Model results

Results from the horizontal model (Eq. 9) for lagoon–sea water exchange are presented in Fig. 9. In general, there was an abrupt increase in the observed $^{224}Ra_{ex}/^{223}$Ra activity ratio within a few meters of the lagoon boundary, due to the relatively more rapid ingrowth of ^{224}Ra with respect to ^{223}Ra, followed by an abrupt decrease in the activity ratio, in which ^{224}Ra reached equilibrium with sediment-surfaces while ^{223}Ra continued to be produced, until the dissolved activity of both isotopes was balanced by production and decay ($^{224}Ra_{ex}/^{223}$Ra = 16.7; Table 2). Model best-fit horizontal advective velocities decreased from 85 to 30 to 20 cm d^{-1} for May, June, and July, respectively (Fig. 9), following the decreasing hydraulic gradient (Table 4). The two transects sampled in May (over 250 m apart) have equal advective velocities from the modeled $^{224}Ra_{ex}/^{223}$Ra activity ratios, suggesting that the flow of lagoon water through the beach was prevalent along La Palme lagoon and the beach of La

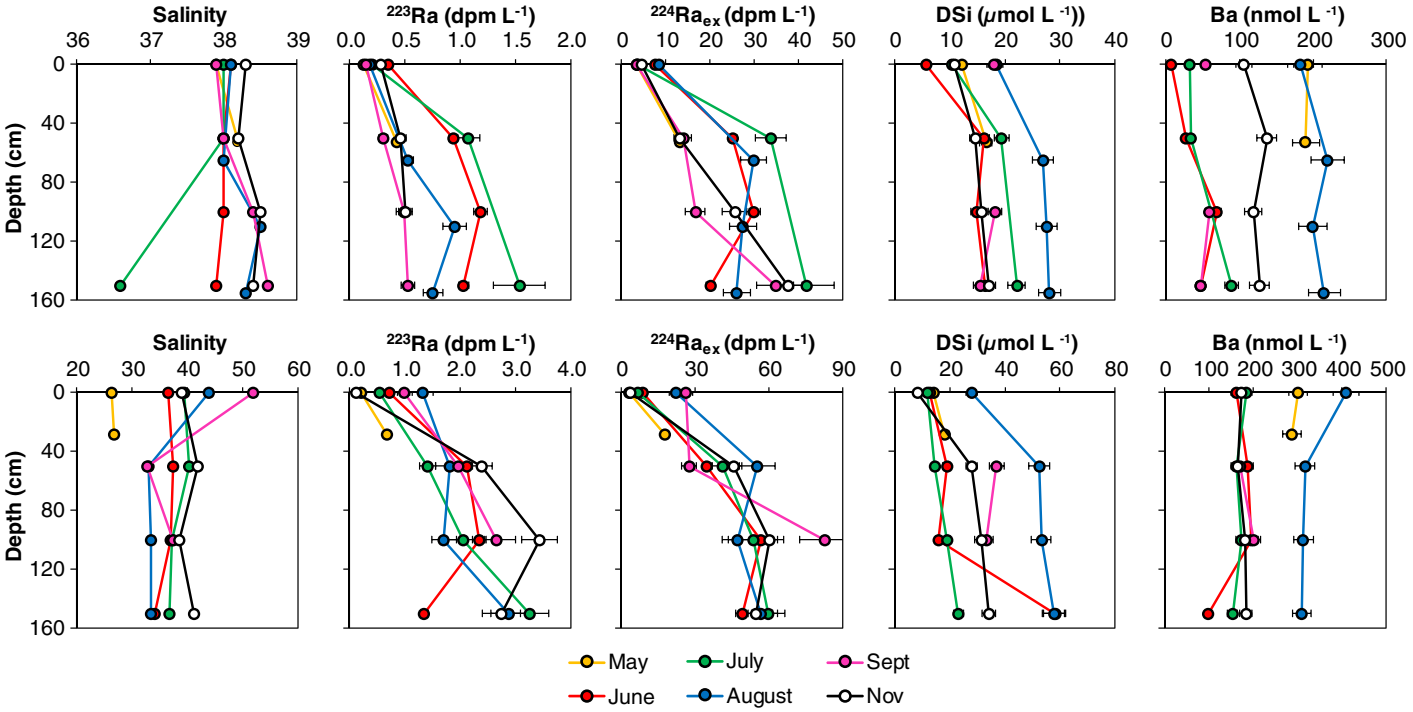

Fig. 7. Vertical distribution of salinity, ^{223}Ra, $^{224}Ra_{ex}$, DSi, and Ba in pore-water samples collected closest to the Mediterranean Sea (top) and closest to the lagoon (bottom), arranged by sampling season.

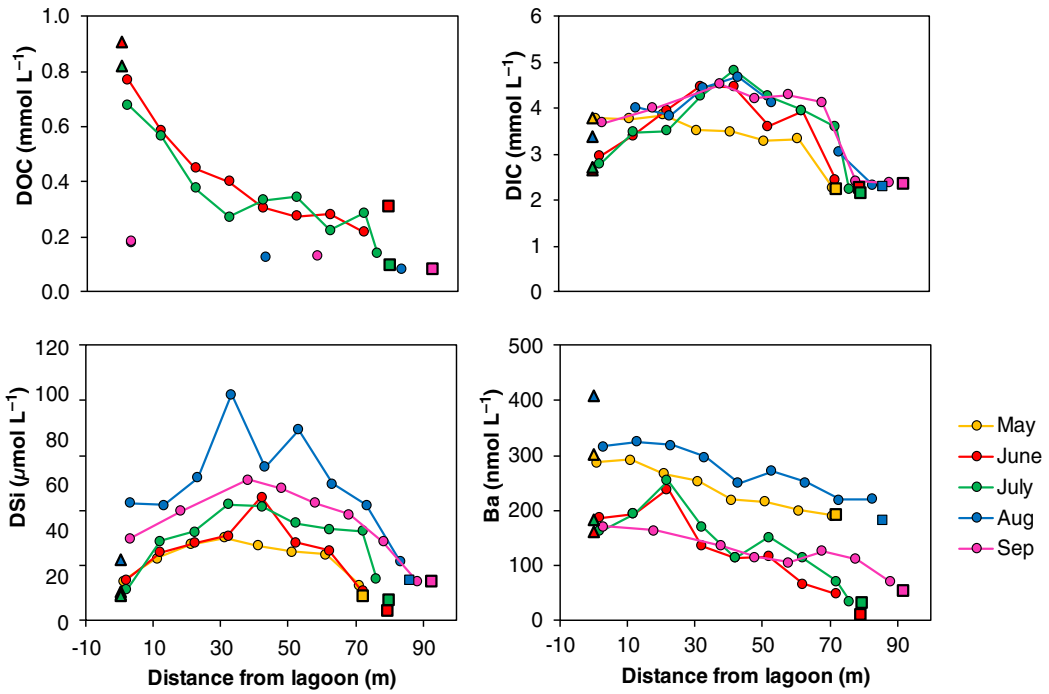

Fig. 8. Spatial distribution of shallow pore-water (50 cm depth; circles) DOC, DIC, DSi, and Ba with respect to lagoon surface water (filled triangle) and Mediterranean Sea (filled square) endmembers. Note that November is not included and only a limited number of samples were analyzed for DOC in May, August, and September.

Franqui during this high-water level period. Therefore, during May, pore-water residence times were on the order of hours close to the lagoon edge (~ 1 m), several days within 10 m of the lagoon and several weeks in the center of the beach. Advective linear velocities are converted to water fluxes considering a mean sediment porosity of 0.38 (Table 5) and an

Table 5. Parameters used in the 1-D reactive-transport model. Note that the term K is only interpolated for the horizontal model. The vertical model uses the term $[P/(1 + K)]$ determined from sediment equilibration experiments for seawater salinity. The radionuclide activity of the Mediterranean Sea and lagoon surface endmember is taken as the value measured for each respective sampling campaign

Term	Definition	Value	Uncertainty	Units
φ	Porosity	0.38	0.01	—
ρ	Sediment density	2.65	—	g cm^{-3}
P_{222}	^{222}Rn production	160	20	dpm L^{-1}
P_{223}	^{223}Ra production	10.6	1.0	dpm L^{-1}
P_{224}	^{224}Ra production	176	25	dpm L^{-1}
K	Ra partition coefficient	Linear interpolation from salinity distribution*	—	—
Δx	Change in distance	Measured from boundary condition	—	m
λ_{222}	^{222}Rn decay constant	0.181	—	d^{-1}
λ_{223}	^{223}Ra decay constant	0.061	—	d^{-1}
λ_{224}	^{224}Ra decay constant	0.193	—	d^{-1}
A_{sea}^{222}	^{222}Rn coastal Mediterranean Sea	4–9	20–40%	dpm L^{-1}
A_{sea}^{223}	^{223}Ra coastal Mediterranean Sea	0.1–0.3	7–9%	dpm L^{-1}
A_{sea}^{224}	^{224}Ra coastal Mediterranean Sea	3.4–8.3	5–9%	dpm L^{-1}
A_{lagoon}^{223}	^{223}Ra lagoon surface water	0.1–1.3	7–14%	dpm L^{-1}
A_{lagoon}^{224}	^{224}Ra lagoon surface water	3.1–26	6–14%	dpm L^{-1}
v	1-D advection velocity	Modeled from curve fitting	15%	m d^{-1}

*K is linearly interpolated between values of 1.5 and 2.9 for salinities of 27–38.

exchange zone depth of 1.0 m (Fig. 7). Volumetric water fluxes for May, June, and July are therefore between 0.1 and 0.3 m^3 d^{-1} m^{-1} of shoreline.

We can qualitatively compare our horizontal 1-D reactive-transport model results to the observed changes in pore-water salinity with time (Fig. 4). Changes in pore-water salinity are explained by mixing between current high-salinity lagoon waters and older (fresher) lagoon waters, driven laterally toward the sea from a positive hydraulic gradient (Table 4). The pore-water salinity profile observed on 22 June persisted 14 d later to 06 July, as the lagoon water level decreased (Table 4) and increased in salinity (37 to 39). On 06 July, the lower salinity endmember from May (~ 25) was observed up to 42 m away from the lagoon, an absolute difference of 6 m (seaward) from 22 June. The difference in the lower salinity plumes horizontal position across the beach corresponds to an integrated horizontal flow velocity of ~ 43 cm d^{-1} (6 m/14 d). From 30 August to 25 September, the low-salinity plume reversed direction; the plume was displaced 11 m toward the lagoon (~ 40 cm d^{-1}).

Vertical profiles (Eq. 7; derived from ^{223}Ra) displayed significant temporal variability, with model best-fit vertical advective velocities equal to 30, 14, 10, 25, 55, and 52 cm d^{-1} for May, June, July, August, September, and November, respectively (e.g., Fig. 10). Estimates derived from ^{222}Rn equal 30 and 90 cm d^{-1} for June and November (Fig. 10), in relative agreement with ^{223}Ra, despite integrating over different time-scales. $^{224}Ra_{ex}$ model results are linearly correlated to estimates from ^{223}Ra (slope = 0.92). Scaling the ^{223}Ra best-fit vertical advective velocities to the width of the swash-zone impacted by seawater circulation (5 m into the beach-face and 5 m into the sea) and considering a mean porosity of 0.38 result in volumetric seawater circulation fluxes between 0.4 and 2.1 m^3 d^{-1} m^{-1} of shoreline. We note that the seawater circulation fluxes for September and November may easily be a factor of two larger, considering the width of the beach impacted by wave setup, from the observed pore-water salinity distribution (Fig. 4).

The Mediterranean beach studied here has a minor tidal range (~ 20–30 cm); therefore, we can compare the above results to other studies conducted in areas with significant tidal ranges to qualitatively assess the role of tidal pumping as a driver of both lagoon–sea water exchange and seawater circulation. Lagoon–sea water exchange fluxes (0.1–0.3 m^3 d^{-1} m^{-1} of shoreline) are an order of magnitude lower than those obtained from higher energy tidal environments subject to exchange through a permeable barrier (e.g., 2.6–5.7 m^3 m^{-1} of shoreline per tide for Cabretta Beach, Georgia; Evans and Wilson 2017). The advective linear velocity estimated for May is similar to rates in a porous limestone coral-reef environment (100 cm d^{-1}; Santos et al. 2010). Larger tidal ranges produce greater water level differences between coastal lagoons and the coastal sea, effectively increasing the hydraulic gradient and therefore SGD rate.

The volumetric flux of seawater circulation estimated here for the swash-zone (0.4–2.1 m^3 d^{-1} m^{-1} of shoreline) is lower than modeling estimates of wave-swash–induced infiltration

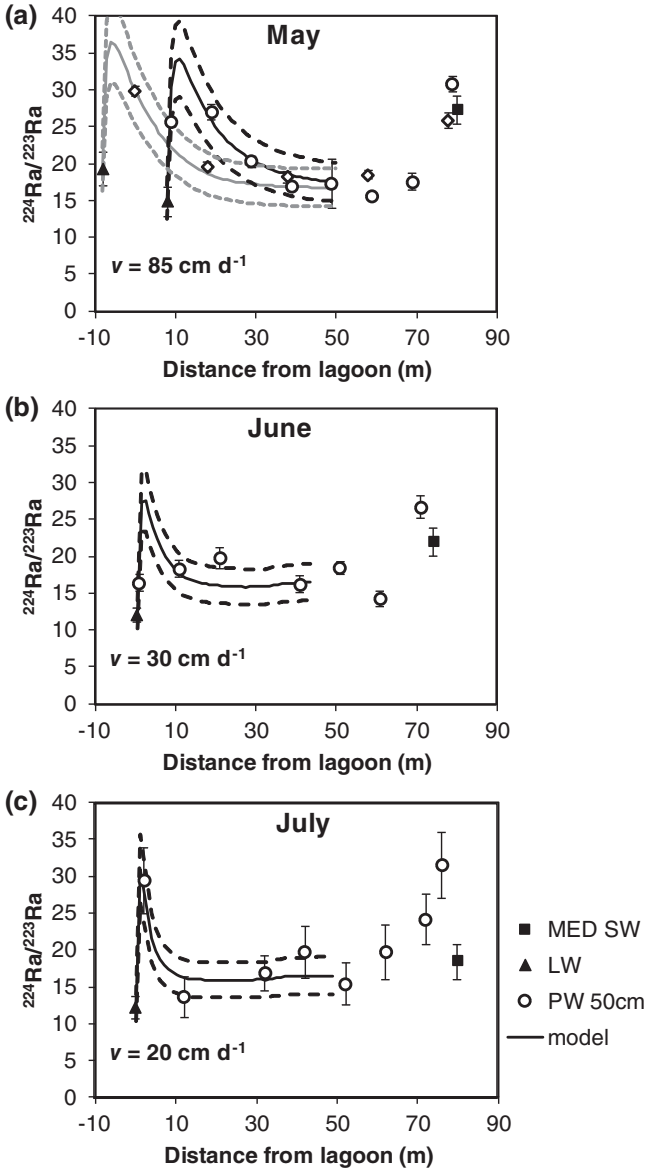

Fig. 9. Distribution of shallow pore-water (≤ 50 cm) $^{224}Ra_{ex}/^{223}Ra$ activity ratios and corresponding results from the $^{224}Ra_{ex}/^{223}Ra$ 1-D horizontal reactive-transport model for May (a), June (b) and July (c) 2017. MED SW = Mediterranean surface water endmember; LW = lagoon surface water endmember. Note that Transect 2 is included in May, with samples depicted as diamonds and model results as gray lines (**a**); T1 is offset during May for clarity. The solid black line is the model run with the lagoon water set as the boundary condition (A_o). Dashed lines represent ± 15% model uncertainty. Model results do not extend farther than 40 m from the lagoon endmember.

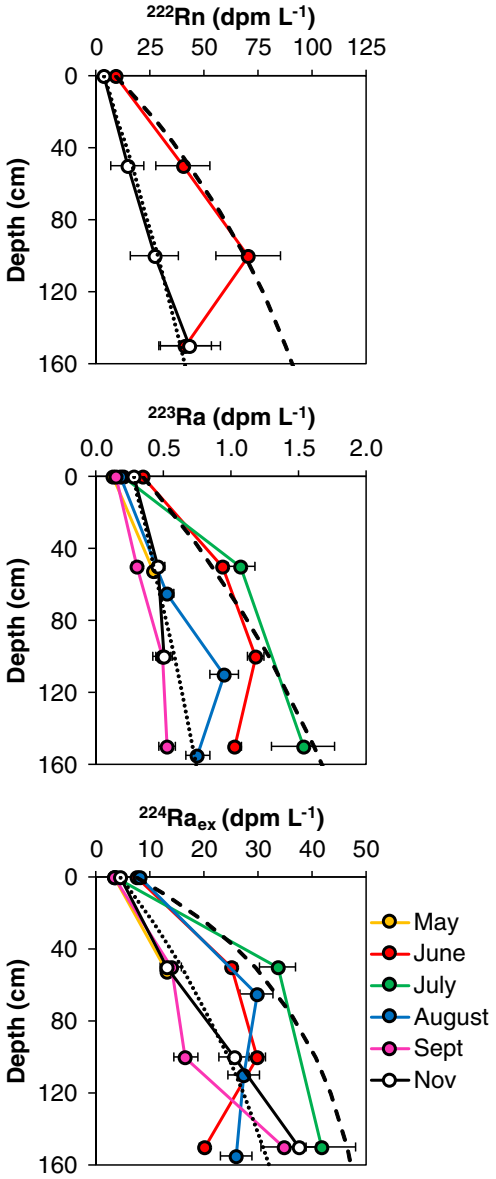

Fig. 10. Vertical distribution of ^{222}Rn, ^{223}Ra, and $^{224}Ra_{ex}$ in pore-water samples collected closest to the Mediterranean Sea. The thick dashed line is the 1-D vertical reactive transport model result for June (^{222}Rn v = 30 cm d^{-1}; ^{223}Ra v = 14 cm d^{-1}; ^{224}Ra v = 14 cm d^{-1}), and the thin dashed line is the vertical model result for November (^{222}Rn v = 90 cm d^{-1}; ^{223}Ra v = 52 cm d^{-1}; ^{224}Ra v = 35 cm d^{-1}).

to the unsaturated zone of a sandy beach (1.6 m^3 m^{-1} of shoreline per tidal cycle) (Heiss et al. 2014) and is an order of magnitude lower than the highly energetic Aquitanian French coastline (~ 15.2 m^3 m^{-1} of shoreline per tidal cycle), driven by tidal pumping and wave setup (Charbonnier et al. 2013). Large tidal variations drive greater amounts of seawater into permeable sediments; tidal pumping is likely more significant than wave or wind setup in tidal environments with limited fetch (Bokuniewicz et al. 2015).

Physical drivers of exchange

Lagoon–sea water exchange

Lagoon–sea water exchange is driven by the pressure-induced hydraulic gradient between the water level of the lagoon and the water level of the Mediterranean Sea. It is apparent that as the lagoon water level decreased from spring through summer, the hydraulic gradient between the lagoon

Table 6. Summary of Fisher's *F* test (Pr > F, df = 3) multiple linear regression model results for seawater circulation through the swash-zone, with corresponding regression coefficients (R^2). Seawater circulation advective velocities (dependent variable) are determined from the ^{223}Ra reactive-transport model. Wind speed and wind direction are the variables used in the "wind" regression; wind setup and wave runup are the variables used in the "waves" regression. Statistically significant model results are indicated in bold

Time (h)	Wind—R^2	Wind—Pr > F	Waves—R^2	Waves—Pr > F
6	0.78	0.10	**0.87**	**0.05**
12	0.79	0.10	0.75	0.12
24	0.64	0.21	0.67	0.19
48	**0.92**	**0.02**	0.09	0.86
72	**0.87**	**0.05**	0.20	0.86
168	0.20	0.71	0.38	0.49
336	0.20	0.71	0.24	0.66

and the Mediterranean Sea decreased (Table 4), resulting in a slower flow of water through the beach. Qualitative flow estimates from Darcy's law ($Q = -k_h \times i$), considering a hydraulic conductivity (k_h) on the order of 10^{-2} to 10^{-3} m s^{-1} for clean sands (Freeze and Cherry 1979) and the hydraulic gradient between the lagoon and the sea (*i*; Table 4) results in horizontal flow velocities on the order of ~ 100 cm d^{-1}. The absolute value of the Darcy flux should not be overly interpreted here, as we do not have detailed information on water table elevation (few point measurements) and sediment hydraulic conductivity (assumed values). Nevertheless, this exercise is useful to constrain the relative magnitude of the horizontal flow velocity to that of the horizontal reactive-transport model.

Seawater circulation

Vertical flushing velocities were highly variable over the 6-month sampling campaign (Fig. 10). Variability in vertical flushing can change with wave height, wave period, and wave direction, all of which are a function of the prevailing wind speed and direction. According to the results from the multiple linear-regression model (Ancillary Parameters section), wind speed and direction significantly explain the temporal variability in vertical flushing velocities. Regression coefficients are strongest for the 48 and 72 h binned averages (R^2 = 0.87 and 0.92, F = 0.02 and 0.05, df = 3; Table 6). Regression coefficients are weaker for the 6–24 h binned averages (R^2 = 0.64–0.79, $F \geq 0.1$, df = 3); no correlation is observed for the 1- and 2-week binned averages (R^2 = 0.2). The significant relationships over the 48 and 72 h intervals display the "memory effect" that Ra and Rn isotopes have in integrating water exchange fluxes over the time-scale of the radionuclide half-life. In contrast, wind setup and wave runup (Eqs. 2–5) significantly explain the temporal variability in vertical flushing for only the 6 h binned average (R^2 = 0.87, F = 0.05, df = 3; Table 6). Several hours may be needed for winds to produce waves in the Mediterranean Sea; however, only a few hours may be needed for waves to affect pore waters, both of which are highly dependent upon direction.

Biogeochemical significance

Lagoon–sea water exchange and seawater circulation flow paths drive early diagenetic nutrient mineralization (Charbonnier et al. 2013) and sediment weathering reactions (Ehlert et al. 2016). Here, we provide a first-order estimate of solute fluxes driven by lagoon–sea water exchange during high water conditions, assuming that flow through the barrier beach was ultimately supplied to the Mediterranean Sea. Lagoon–sea water exchange is a net water source and may therefore be a net solute flux to the coastal Mediterranean Sea, depending upon biogeochemical reactions (Cook et al. 2018*b*). Solute concentrations measured at ~ 20 m distance from the sea (Table 7) are used as the endmember to estimate lagoon–sea water exchange solute fluxes. At this distance, we assume negligible dilution from mixing with seawater (Fig. 4) and that most of the biogeochemical transformations have occurred (Fig. 8). Corresponding DSi, DIC, and Ba fluxes equal 10 mmol Si d^{-1} m^{-1}, 1100 mmol C d^{-1} m^{-1}, and 70 μmol Ba d^{-1} m^{-1} of shoreline during May 2017 (Table 7). Solute fluxes decrease from June to July (Table 7) as a consequence of reduced flow (Fig. 9).

The lagoon–sea water exchange DIC flux is ~ 70–200 mmol m^{-2} d^{-1} assuming a 5-m wide seepage face; this flux is within the global range of DIC inputs from SGD (~ 10–2000 mmol m^{-2} d^{-1}) summarized by Sadat-Noori et al. (2016). DIC inputs from lagoon–sea water exchange can lead to coastal ocean acidification (Robinson et al. 2018), which may explain the relatively low pH values measured in the coastal Mediterranean Sea during the spring (pH = 8.03 in May, pH = 8.20 in June, and pH = 8.25 in September; Supporting Information). With regard to Ba, dissolved concentrations are typically ~ 40 nmol L^{-1} in the Mediterranean Sea (Jacquet et al. 2016). Local Ba inputs from lagoon–sea water exchange may alter local Ba biogeochemical cycling; further work is required to understand the role of SGD as a source of Ba to the Mediterranean Sea.

Adjacent to the Mediterranean Sea, pore waters with the same salinity as seawater were enriched in DIC (25–110 μmol L^{-1} C) and DSi (4–11 μmol L^{-1} Si) over surface waters, whereas Ba concentrations were relatively uniform (Fig. 7). Linear Ba profiles suggest that seawater circulation in the swash-zone is not a net source of Ba to the coastal sea. We may estimate solute fluxes in the swash-zone by multiplying the net solute concentration (enrichment over Mediterranean seawater) by the volume of seawater circulation (Cook et al. 2018*b*). Seawater-circulation–driven DIC fluxes through the swash-zone are between 14 and 220 mmol C d^{-1} m^{-1} of shoreline (Table 7), possibly as a consequence of carbonate

Table 7. Summary of water exchange, DSi (mmol m^{-1} d^{-1}), DIC (mmol m^{-1} d^{-1}), and Ba (μmol m^{-1} d^{-1}) fluxes, arranged by sampling season. Lagoon–sea water exchange is only considered for May, June, and July. Swash-zone seawater circulation flushing rates are derived from ^{223}Ra profiles; Ba fluxes are not estimated for seawater circulation

Date	Flushing rate (cm d^{-1})	Flushing rate (m^3 d^{-1} m^{-1})	Concentration (μmol L^{-1} Si)	Si flux (mmol m^{-1} d^{-1})	Concentration (μmol L^{-1} C)	C flux (mmol m^{-1} d^{-1})	Concentration (nmol L^{-1} Ba)	Ba flux (μmol m^{-1} d^{-1})
*Horizontal transport (lagoon)**								
09 May	85	0.3	31	10	3280	1100	220	70
22 Jun	30	0.1	35	4	3610	410	120	10
06 Jul	20	0.1	44	3	4260	320	150	10
Seawater circulation†								
09 May	30	1.1	4	5	25	29	—	—
22 Jun	14	0.5	11	6	27	14	—	—
06 Jul	10	0.4	9	3	53	20	—	—
30 Aug	25	1.0	9	8	52	50	—	—
25 Sep	55	2.1	—	—	—	—	—	—
17 Nov	52	2.0	4	7	110	220	—	—

*Exchange zone depth = 1 m; DSi, DIC, and Ba concentrations taken at ~ x = 20 m from the sea.
†Swash-zone width = 10 m; DSi and DIC concentrations are net enrichments over coastal Mediterranean Sea surface endmembers.

mineral weathering, in addition to POC and DOC consumption (Fig. 7). Seawater circulation-driven DSi fluxes through the swash-zone are between 3 and 8 mmol Si d^{-1} m^{-1} of shoreline (Table 7).

During November 2016, SGD was estimated to supply a DSi flux of 2.4 ± 1.4 mol Si d^{-1} m^{-1} of shoreline for La Franqui based on offshore transects that were conducted in the coastal seas (Tamborski et al. 2018). This DSi flux was hypothesized to be driven by both lagoon–sea water exchange (relatively high water levels) and seawater circulation (Tamborski et al. 2018); this flux is 2–3 orders of magnitude larger than the DSi fluxes calculated here for the swash-zone (Table 7). The DSi flux of Tamborski et al. (2018) may include additional, unaccounted for flow paths between the swash-zone (this study) and 300 m offshore, where the surface water transects to quantify SGD originated (fig. 6 of Tamborski et al. 2018). Water depth is ≤ 5 m over 300 m from shore; seawater circulation through this shallow zone, over a large area (~ 3 km^2), may thus be an adequate source of DSi (and Ra) offshore of La Franqui. To reconcile the difference in the DSi flux from this study and Tamborski et al. (2018), we hypothesize that offshore seawater circulation may supply a DSi flux on the order of 1–2 mol Si d^{-1} m^{-1} of shoreline. Although seawater circulation is relatively small in supplying DSi from the narrow swash-zone, this flow path may be significant over the larger area of the shallow coastal zone; future research is required to better constrain these coastal solute fluxes.

Conclusions

Various flow paths make up the term SGD (Santos et al. 2012). Individual driving mechanisms are seldom quantified with respect to absolute water fluxes and its associated chemical load to the sea (Robinson et al. 2018), despite increasing recognition that individual flow paths may have unique geochemical signatures (Tamborski et al. 2017; Rodellas et al. 2018). In this study, we present a simple Ra isotope methodology, which builds upon preexisting analytical measurements and theoretical models to explicitly quantify (1) lagoon–sea water exchange through a permeable sand barrier and (2) seawater circulation in the swash-zone of the sand barrier. Multiple methods are recommended to determine the production (P) and partitioning (K) of Ra between sediment surfaces and solution in order to properly model 1-D Ra transport. This methodology provides a framework where future researchers may discriminate between unique SGD flow paths, which in turn will help improve solute flux estimates and our understanding of coastal biogeochemical cycles.

Repeated measurements at a Mediterranean barrier beach site show that lagoon–sea water exchange varies in response to the changing hydraulic gradient between the lagoon and the sea. This flow path is a net water flux which supplies the greatest DSi (10 mmol d^{-1} m^{-1}), DIC (1100 mmol d^{-1} m^{-1}),

and Ba (70 μmol d^{-1} m^{-1}) flux to the coastal Mediterranean Sea during high lagoon water-level periods. The DIC flux from lagoon–sea water exchange is comparable to other SGD studies and suggests that this vector may enhance coastal ocean acidification in the Mediterranean Sea (Sadat-Noori et al. 2016). We conclude that coastal lagoons represent a significant source of new DIC and Ba to the Mediterranean Sea during high-water–level periods and are likely an important source for other dissolved chemical elements as well. Solute fluxes may significantly decrease during the dry season (summer), when lagoon surface water levels decrease. As a result, this seasonal vector should be considered in future coastal zone chemical budgets.

Seawater circulation through the swash-zone varies in response to short-term (hours to days) changes in regional wind and wave regimes. This is one of the first studies to quantitatively link a seawater circulation flux to its physical driving mechanism(s), tidal pumping notwithstanding. This vector is relatively minor in transferring DSi and DIC to the Mediterranean Sea during the studied period (May–November 2017), whereas Ba inputs are negligible. It remains to be seen how significant these individual flow paths are in transferring other chemical elements, such as N and P, to the coastal Mediterranean Sea. Further work is required to understand the importance of seawater circulation along the shallow nearshore coastal zone (~ 0–300 m offshore) to the Mediterranean Sea.

References

Anschutz, P., T. Smith, A. Mouret, J. Deborde, S. Bujan, D. Poirier, and P. Lecroart. 2009. Tidal sands as biogeochemical reactors. Estuar. Coast. Shelf Sci. **84**: 84–90. doi:10.1016/j.ecss.2009.06.015

Bacon, M. P., and R. F. Anderson. 1982. Distribution of thorium isotopes between dissolved and particulate forms in the deep sea. J. Geophys. Res. **87**: 2045. doi:10.1029/JC087iC03p02045

Barnes, R. S. K. 1980. Coastal lagoons. Cambridge Univ. Press. doi:10.1016/0092-8674(80)90540-1

Beck, A. J., and M. A. Cochran. 2013. Controls on solid-solution partitioning of radium in saturated marine sands. Mar. Chem. **156**: 38–48. doi:10.1016/j.marchem.2013.01.008

Bokuniewicz, H., and B. Pavlik. 1990. Groundwater seepage along a barrier-Island. Biogeochemistry **10**: 257–276. doi:10.1007/BF00003147

Bokuniewicz, H., J. K. Cochran, J. Garcia-Orellana, V. Rodellas, J. W. Daniel, and C. Heilbrun. 2015. Intertidal percolation through beach sands as a source of 224.223Ra to Long Island Sound, New York and Connecticut, United States. J. Mar. Res. **73**: 123–140. doi:10.1357/002224015816665570

Burnett, W. C., H. Bokuniewicz, M. Huettel, W. S. Moore, and M. Taniguchi. 2003. Groundwater and pore water inputs to the coastal zone. Biogeochemistry **66**: 3–33. doi:10.1023/B:BIOG.0000006066.21240.53

Cai, P., X. Shi, W. S. Moore, and M. Dai. 2012. Measurement of ^{224}Ra:^{228}Th disequilibrium in coastal sediments using a delayed coincidence counter. Mar. Chem. **138–139**: 1–6. doi:10.1016/j.marchem.2012.05.004

Cai, P., X. Shi, W. S. Moore, S. Peng, G. Wang, and M. Dai. 2014. ^{224}Ra:^{228}Th disequilibrium in coastal sediments: Implications for solute transfer across the sediment-water interface. Geochim. Cosmochim. Acta **125**: 68–84. doi:10.1016/j.gca.2013.09.029

Chanton, J., W. Burnett, H. Dulaiova, D. Corbett, and M. Taniguchi. 2003. Seepage rate variability in Florida Bay driven by Atlantic tidal height. Biogeochemistry **66**: 187–202. doi:10.1023/B:BIOG.0000006168.17717.91

Charbonnier, C., P. Anschutz, D. Poirier, S. Bujan, and P. Lecroart. 2013. Aerobic respiration in a high-energy sandy beach. Mar. Chem. **155**: 10–21. doi:10.1016/j.marchem.2013.05.003

Charette, M. A., and M. C. Allen. 2006. Precision ground water sampling in coastal aquifers using a direct-push, shielded-screen well-point system. Ground Water Monit. Remediat. **26**: 87–93. doi:10.1111/j.1745-6592.2006.00076.x

Cochran, J. K., A. E. Carey, E. R. Sholkovitz, and L. D. Surprenant. 1986. The geochemistry of uranium and thorium in coastal marine sediments and sediment pore waters. Geochim. Cosmochim. Acta **50**: 663–680. doi:10.1016/0016-7037(86)90344-3

Colbert, S. L., and D. E. Hammond. 2008. Shoreline and seafloor fluxes of water and short-lived Ra isotopes to surface water of San Pedro Bay, CA. Mar. Chem. **108**: 1–17. doi:10.1016/j.marchem.2007.09.004

Cook, P. G., V. Rodellas, A. Andrisoa, and T. C. Stieglitz. 2018*a*. Exchange across the sediment-water interface quantified from porewater radon profiles. J. Hydrol. **559**: 873–883. doi:10.1016/J.JHYDROL.2018.02.070

Cook, P. G., V. Rodellas, and T. C. Stieglitz. 2018*b*. Quantifying surface water, porewater, and groundwater interactions using tracers: Tracer fluxes, water fluxes, and end-member concentrations. Water Resour. Res. **54**: 2452–2465. doi:10.1002/2017WR021780

Copenhaver, S. A., S. Krishnaswami, K. K. Turekian, N. Epler, and J. K. Cochran. 1993. Retardation of U-238 and TH-232 decay chain radionuclides in long-island and Connecticut aquifers. Geochim. Cosmochim. Acta **57**: 597–603. doi:10.1016/0016-7037(93)90370-c

Corbett, D. R., K. Dillon, and W. Burnett. 2000. Tracing groundwater flow on a Barrier Island in the north-east Gulf of Mexico. Estuar. Coast. Shelf Sci. **51**: 227–242. doi:10.1006/ecss.2000.0606

Dean, R. G., and R. A. Dalrymple. 2004. Coastal processes with engineering applications. Cambridge Univ. Press.

Dimova, N., P. Ganguli, P. Swarzenski, J. Izbicki, and D. O'Leary. 2017. Hydrogeologic controls on chemical transport

at Malibu Lagoon, CA: Implications for land to sea exchange in coastal lagoon systems. J. Hydrol. Reg. Stud. **11**: 219–233. doi:10.1016/j.ejrh.2016.08.003

Dulaiova, H., M. E. Gonneea, P. B. Henderson, and M. A. Charette. 2008. Geochemical and physical sources of radon variation in a subterranean estuary—implications for groundwater radon activities in submarine groundwater discharge studies. Mar. Chem. **110**: 120–127. doi:10.1016/j.marchem.2008.02.011

Ehlert, C., A. Reckhardt, J. Greskowiak, B. T. P. Liguori, P. Boning, R. Paffrath, H. J. Brumsack, and K. Pahnke. 2016. Transformation of silicon in a sandy beach ecosystem: Insights from stable silicon isotopes from fresh and saline groundwaters. Chem. Geol. **440**: 207–218. doi:10.1016/j.chemgeo.2016.07.015

Evans, T. B., and A. M. Wilson. 2017. Submarine groundwater discharge and solute transport under a transgressive Barrier Island. J. Hydrol. **547**: 97–110. doi:10.1016/J.JHYDROL.2017.01.028

Fisher, N. S., P. Bjerregaard, and S. W. Fowler. 1983. Interactions of marine plankton with transuranic elements. 1. Biokinetics of neptunium, plutonium, americium, and californium in phytoplankton. Limnol. Oceanogr. **28**: 432–447. doi:10.4319/lo.1983.28.3.0432

Freeze, R. A., and J. A. Cherry. 1979. Groundwater. Prentice-Hall.

Garcia-Solsona, E., J. Garcia-Orellana, P. Masque, and H. Dulaiova. 2008. Uncertainties associated with Ra-223 and Ra-224 measurements in water via a delayed coincidence counter (RaDeCC). Mar. Chem. **109**: 198–219. doi:10.1016/j.marchem.2007.11.006

Gonneea, M. E., P. J. Morris, H. Dulaiova, and M. A. Charette. 2008. New perspectives on radium behavior within a subterranean estuary. Mar. Chem. **109**: 250–267. doi:10.1016/j.marchem.2007.12.002

Gonneea, M. E., A. E. Mulligan, and M. A. Charette. 2013. Seasonal cycles in radium and barium within a subterranean estuary: Implications for groundwater derived chemical fluxes to surface waters. Geochim. Cosmochim. Acta **119**: 164–177. doi:10.1016/j.gca.2013.05.034

Goodridge, B. M., and J. M. Melack. 2014. Temporal evolution and variability of dissolved inorganic nitrogen in beach pore water revealed using radon residence times. Environ. Sci. Technol. **48**: 14211–14218. doi:10.1021/es504017j

Heiss, J. W., W. J. Ullman, and H. A. Michael. 2014. Swash zone moisture dynamics and unsaturated infiltration in two sandy beach aquifers. Estuar. Coast. Shelf Sci. **143**: 20–31. doi:10.1016/J.ECSS.2014.03.015

Honeyman, B. D., L. S. Balistrieri, and J. W. Murray. 1988. Oceanic trace metal scavenging: The importance of particle concentration. Deep-Sea Res. Part A. Oceanogr. Res. Pap. **35**: 227–246. doi:10.1016/0198-0149(88)90038-6

Jacquet, S. H. M., C. Monnin, V. Riou, L. Jullion, and T. Tanhua. 2016. A high resolution and quasi-zonal transect of dissolved Ba in the Mediterranean Sea. Mar. Chem. **178**: 1–7. doi:10.1016/J.MARCHEM.2015.12.001

Kiro, Y., Y. Yechieli, C. I. Voss, A. Starinsky, and Y. Weinstein. 2012. Modeling radium distribution in coastal aquifers during sea level changes: The Dead Sea case. Geochim. Cosmochim. Acta **88**: 237–254. doi:10.1016/j.gca.2012.03.022

Kiro, Y., Y. Weinstein, A. Starinsky, and Y. Yechieli. 2013. Groundwater ages and reaction rates during seawater circulation in the Dead Sea aquifer. Geochim. Cosmochim. Acta **122**: 17–35. doi:10.1016/j.gca.2013.08.005

Kiro, Y., Y. Weinstein, A. Starinsky, and Y. Yechieli. 2015. Application of radon and radium isotopes to groundwater flow dynamics: An examples from the Dead Sea. Chem. Geol. **411**: 155–171. doi:10.1016/j.chemgeo.2015.06.014

Krest, J. M., and J. W. Harvey. 2003. Using natural distributions of short-lived radium isotopes to quantify groundwater discharge and recharge. Limnol. Oceanogr. **48**: 290–298. doi:10.4319/lo.2003.48.1.0290

Krishnaswami, S., W. C. Graustein, K. K. Turekian, and J. F. Dowd. 1982. Radium, thorium and radioactive lead isotopes in groundwaters—application to the in situ determination of adsorption-desorption rate constants and retardation factors. Water Resour. Res. **18**: 1663–1675. doi:10.1029/WR018i006p01663

Krishnaswami, S., R. Bhushan, and M. Baskaran. 1991. Radium isotopes and 222Rn in shallow brines, Kharaghoda (India). Chem. Geol. Isot. Geosci. Sect. **87**: 125–136. doi:10.1016/0168-9622(91)90046-Y

Li, L., D. A. Barry, F. Stagnitti, and J. Y. Parlange. 1999. Submarine groundwater discharge and associated chemical input to a coastal sea. Water Resour. Res. **35**: 3253–3259. doi:10.1029/1999WR900189

Luo, S., T.-L. Ku, R. Roback, M. Murrell, and T. McLing. 2000. In-situ radionuclide transport and preferential groundwater flows at INEEL (Idaho): Decay-series disequilibrium studies. Geochim. Cosmochim. Acta **64**: 867–881. doi:10.1016/S0016-7037(99)00373-7

Michael, H. A., M. A. Charette, and C. F. Harvey. 2011. Patterns and variability of groundwater flow and radium activity at the coast: A case study from Waquoit Bay, Massachusetts. Mar. Chem. **127**: 100–114. doi:10.1016/j.marchem.2011.08.001

Moore, W. S., and R. Arnold. 1996. Measurement of Ra-223 and Ra-224 in coastal waters using a delayed coincidence counter. J. Geophys. Res. **101**: 1321–1329. doi:10.1029/95JC03139

Niencheski, L. F. H., H. L. Windom, W. S. Moore, and R. A. Jahnke. 2007. Submarine groundwater discharge of nutrients to the ocean along a coastal lagoon barrier, southern Brazil. Mar. Chem. **106**: 546–561. doi:10.1016/j.marchem.2007.06.004

Porcelli, D. 2008. Chapter 4 investigating groundwater processes using U- and Th-series nuclides. Radioact. Environ. **13**: 105–153. doi:10.1016/S1569-4860(07)00004-6

Porcelli, D., and P. W. Swarzenski. 2003. The behavior of U- and Th-series nuclides in groundwater. Rev. Mineral. Geochem. **52**: 317–361. doi:10.2113/0520317

Rapaglia, J., E. Di Sipio, H. Bokuniewicz, G. M. Zuppi, L. Zaggia, A. Galgaro, and A. Beck. 2010. Groundwater connections under a barrier beach: A case study in the Venice Lagoon. Cont. Shelf Res. **30**: 119–126. doi:10.1016/j.csr.2009.10.001

Roberts, K. A., C. Xu, C.-C. Hung, M. H. Conte, and P. H. Santschi. 2009. Scavenging and fractionation of thorium vs. protactinium in the ocean, as determined from particle–water partitioning experiments with sediment trap material from the Gulf of Mexico and Sargasso Sea. Earth Planet. Sci. Lett. **286**: 131–138. doi:10.1016/J.EPSL.2009.06.029

Robinson, C., L. Li, and H. Prommer. 2007. Tide-induced recirculation across the aquifer-ocean interface. Water Resour. Res. **43**: W07428. doi:10.1029/2006WR005679

Robinson, C. E., P. Xin, I. R. Santos, M. A. Charette, L. Li, and D. A. Barry. 2018. Groundwater dynamics in subterranean estuaries of coastal unconfined aquifers: Controls on submarine groundwater discharge and chemical inputs to the ocean. Adv. Water Resour. **115**: 315–331. doi:10.1016/J.ADVWATRES.2017.10.041

Rodellas, V., J. Garcia-Orellana, G. Trezzi, P. Masque, T. C. Stieglitz, H. Bokuniewicz, J. K. Cochran, and E. Berdalet. 2017. Using the radium quartet to quantify submarine groundwater discharge and porewater exchange. Geochim. Cosmochim. Acta **196**: 58–73. doi:10.1016/j.gca.2016.09.016

Rodellas, V., T. C. Stieglitz, A. Andrisoa, P. G. Cook, P. Raimbault, J. J. Tamborski, P. van Beek, and O. Radakovitch. 2018. Groundwater-driven nutrient inputs to coastal lagoons: The relevance of lagoon water recirculation as a conveyor of dissolved nutrients. Sci. Total Environ. **642**: 764–780. doi:10.1016/j.scitotenv.2018.06.095

Sadat-Noori, M., D. T. Maher, and I. R. Santos. 2016. Groundwater discharge as a source of dissolved carbon and greenhouse gases in a subtropical estuary. Estuaries Coasts **39**: 639–656. doi:10.1007/s12237-015-0042-4

Santos, I. R., W. C. Burnett, T. Dittmar, I. G. N. A. Suryaputra, and J. Chanton. 2009. Tidal pumping drives nutrient and dissolved organic matter dynamics in a Gulf of Mexico subterranean estuary. Geochim. Cosmochim. Acta **73**: 1325–1339. doi:10.1016/J.GCA.2008.11.029

Santos, I. R., D. V. Erler, D. R. Tait, and B. D. Eyre. 2010. Breathing of a coral cay: Tracing tidally driven seawater recirculation in permeable coral reef sediments. J. Geophys. Res. **115**: C12010. doi:10.1029/2010JC006510

Santos, I. R., B. D. Eyre, and M. Huettel. 2012. The driving forces of porewater and groundwater flow in permeable coastal sediments: A review. Estuar. Coast. Shelf Sci. **98**: 1–15. doi:10.1016/j.ecss.2011.10.024

Schopka, H. H., and L. A. Derry. 2012. Chemical weathering fluxes from volcanic islands and the importance of groundwater: The Hawaiian example. Earth Planet. Sci. Lett. **339–340**: 67–78. doi:10.1016/j.epsl.2012.05.028

Smith, C. G., J. E. Cable, J. B. Martin, and M. Roy. 2008. Evaluating the source and seasonality of submarine groundwater discharge using a radon-222 pore water transport model. Earth Planet. Sci. Lett. **273**: 312–322. doi:10.1016/j.epsl.2008.06.043

Sous, D., L. Petitjean, F. Bouchette, V. Rey, S. Meulé, F. Sabatier, and K. Martins. 2016. Field evidence of swash groundwater circulation in the microtidal rousty beach, France. Adv. Water Resour. **97**: 144–155. doi:10.1016/J.ADVWATRES.2016.09.009

Stieglitz, T. C., P. van Beek, M. Souhaut, and P. G. Cook. 2013. Karstic groundwater discharge and seawater recirculation through sediments in shallow coastal Mediterranean lagoons, determined from water, salt and radon budgets. Mar. Chem. **156**: 73–84. doi:10.1016/j.marchem.2013.05.005

Stockdon, H. F., R. A. Holman, P. A. Howd, and A. H. Sallenger Jr. 2006. Empirical parameterization of setup, swash, and runup. Coast. Eng. **53**: 573–588. doi:10.1016/j.coastaleng.2005.12.005

Sun, Y., and T. Torgersen. 1998*a*. The effects of water content and Mn-fiber surface conditions on ^{224}Ra measurement by ^{220}Rn emanation. Mar. Chem. **62**: 299–306. doi:10.1016/S0304-4203(98)00019-X

Sun, Y., and T. Torgersen. 1998*b*. Rapid and precise measurement method for adsorbed ^{224}Ra on sediments. Mar. Chem. **61**: 163–171. doi:10.1016/S0304-4203(98)00016-4

Tamborski, J. J., J. K. Cochran, and H. J. Bokuniewicz. 2017. Application of ^{224}Ra and ^{222}Rn for evaluating seawater residence times in a tidal subterranean estuary. Mar. Chem. **189**: 32–45. doi:10.1016/j.marchem.2016.12.006

Tamborski, J., and others. 2018. A comparison between water circulation and terrestrially-driven dissolved silica fluxes to the Mediterranean Sea traced using radium isotopes. Geochim. Cosmochim. Acta Theriol. **238**: 496–515. doi:10.1016/J.GCA.2018.07.022

Tricca, A., G. J. Wasserburg, D. Porcelli, and M. Baskaran. 2001. The transport of U- and Th-series nuclides in a sandy unconfined aquifer. Geochim. Cosmochim. Acta **65**: 1187–1210. doi:10.1016/S0016-7037(00)00617-7

Webster, I. T., G. J. Hancock, and A. S. Murray. 1995. Modelling the effect of salinity on radium desorption from sediments. Geochim. Cosmochim. Acta **59**: 2469–2476. doi:10.1016/0016-7037(95)00141-7

Windom, H. L., W. S. Moore, L. F. H. Niencheski, and R. A. Jahnke. 2006. Submarine groundwater discharge: A large, previously unrecognized source of dissolved iron to the South Atlantic Ocean. Mar. Chem. **102**: 252–266. doi:10.1016/J.MARCHEM.2006.06.016

Xin, P., C. Robinson, L. Li, D. A. Barry, and R. Bakhtyar. 2010. Effects of wave forcing on a subterranean estuary. Water Resour. Res. **46**: W12505. doi:10.1029/2010WR009632

ACKNOWLEDGMENTS

This study was funded by ANR MED-SGD (ANR-15-CE01-0004; P.v.I.). The postdoctoral fellowship of Joseph Tamborski and the PhD thesis of

Simon Bejannin are supported by FEDER funded by Europe and Région Occitanie Pyrénées-Méditerranée (SELECT project). Valentí Rodellas acknowledges financial support from the European Union's Horizon 2020 research and innovation program under the Marie Skłodowska-Curie grant agreement 748896. Thomas Stieglitz holds a chair at RAction of the French Agence National de Recherche ANR (ANR-14-ACHN-0007-01, project medLOC) and is supported by the Labex OT-Med (ANR-11-LABEX-0061) funded by the "Investissements d'Avenir" program through the AMIDEX project (ANR-11-IDEX-0001-02). We are grateful to Kattalin Fortuné-Sans and Camille Pfleger (Parc Naturel Régional de la Narbonnaise en Méditerranée), Philippe Dussoullez and Jules Fleury for help with the beach topography survey, and Alain Le Berre (Cerema) for the wave buoy data. We thank Marc Souhaut for technical support in the LEGOS laboratory and at the LAFARA underground laboratory. We thank two anonymous reviewers for their helpful comments on an earlier draft of this manuscript.

Conflict of Interest

None declared.

Submitted 17 September 2018
Revised 08 February 2019
Accepted 11 March 2019

Associate editor: Bradley Eyre